

Phase-Field Modeling of Equilibrium Precipitate Shapes Under the Influence of Coherency Stresses



BHALCHANDRA BHADAK, R. SANKARASUBRAMANIAN,
and ABHIK CHOUDHURY

Coherency misfit stresses and their related anisotropies are known to influence the equilibrium shapes of precipitates. Additionally, mechanical properties of the alloys are also dependent on the shapes of the precipitates. Therefore, in order to investigate the mechanical response of a material which undergoes precipitation during heat treatment, it is important to derive the range of precipitate shapes that evolve. In this regard, several studies have been conducted in the past using sharp-interface approaches where the influence of elastic energy anisotropy on the precipitate shapes has been investigated. In this paper, we propose a diffuse interface approach which allows us to minimize grid-anisotropy-related issues applicable to sharp-interface methods. In this context, we introduce a novel phase-field method where we minimize the functional consisting of the elastic and surface energy contributions while preserving the precipitate volume. Using this technique, we reproduce the shape bifurcation diagrams for the cases of pure dilatational misfit that have been studied previously using sharp-interface methods and then extend them to include interfacial energy anisotropy with different anisotropy strengths which has not been a part of previous sharp-interface models. While we restrict ourselves to cubic anisotropies in both elastic and interfacial energies in this study, the model is generic enough to handle any combination of anisotropies in both the bulk and interfacial terms. Further, we have examined the influence of asymmetry in dilatational misfit strains along with interfacial energy anisotropy on precipitate morphologies.

<https://doi.org/10.1007/s11661-018-4835-5>

© The Minerals, Metals & Materials Society and ASM International 2018

I. INTRODUCTION

PRECIPITATE strengthened alloys are one of the most commonly used materials for high-temperature applications, whereby, the strengthening is achieved through precipitate–dislocation interactions. The mechanical properties of these alloys predominantly depend on precipitate size, morphologies, and their distribution. Thus, there are several experimental studies carried out which focus on the precipitate morphology,^[1,2] their growth and coarsening,^[3–6] strengthening.^[7,8] In this regard, there are two mechanisms, one in which the precipitates are large enough such that there is no coherency between the precipitate and the matrix from which it is formed, and the second in which the precipitates are small such that there is still substantial coherency between the matrix and the precipitate. While

in the former, the interaction of the dislocation with the precipitate is purely physical, in the latter, the coherency stresses around the precipitate also influence the interaction with the precipitate. In both cases, the shape of the precipitate plays an important role in the interaction with the dislocation. Our investigation in this paper will be related to the investigation of shapes of coherent precipitates, more particularly the understanding of the equilibrium morphology of precipitates as a function of the misfits, elastic, and interfacial energy anisotropies.

The first theoretical efforts are from Johnson and Cahn^[9] who predict an equilibrium shape transition of an elastically isotropic misfitting precipitate in a stiffer matrix. The equilibrium shape of a precipitate is determined by minimization under the constraint of constant volume of the precipitate, of the total energy, constituting of the sum of elastic and interfacial energies. The theory proposes the shape transition with size, akin to a second-order phase transition with the shape of the precipitate as an order parameter. The theory analytically predicts the equilibrium shape order parameters as a function of precipitate size whereby for certain conditions, below a critical size there is a unique order parameter describing the shape of the particle and a bifurcation into two or more variants beyond it. In their

BHALCHANDRA BHADAK and ABHIK CHOUDHURY are with the Department of Materials Engineering, Indian Institute of Science, Bangalore 560012, India. Contact e-mail: bhalchandrab@iisc.ac.in R. SANKARASUBRAMANIAN is with the Defence Metallurgical Research Laboratory, Hyderabad 500058, India.

Manuscript submitted April 4, 2018.

Article published online August 2, 2018

work, one of the transitions the authors discuss is the case where, beyond a particular size of a precipitate, a purely circular cross section of a cylindrical precipitate elongates along either of two-orthogonal directions, thereby retaining only a twofold symmetry. This is therefore an example of a symmetry breaking transition.

Voorhees *et al.*^[10] and Thompson *et al.*^[11] give numerical predictions for the equilibrium morphologies of a precipitate in a system with dilatational and tetragonal misfit in an elastically anisotropic medium (cubic anisotropy). In this work, the authors discretize the interface coordinates in terms of the arc-length and use this to write the total energy of the system, that is a sum of the elastic and the interfacial energies. Thereafter, the minimizer of the total integrated energy of the system is described by the one which satisfies the jump condition at the interface. The condition equates the difference of the chemical potential between the phases (which is a function of the uniform diffusion potential in the system) at the interface to the sum total of the elastic configuration and capillarity forces. This balance condition for each of the discretized interface points leads to a set of integro-differential equations, which along with the constraint of constant area leads to the determination of the uniform diffusion potential that satisfies the interface balance conditions at all the coordinates. The solution set for the coordinates thereby constitutes the equilibrium shape of the particle. The method has also been extended into three dimensions (3Ds) in the work by Thompson and Voorhees^[12] and Li *et al.*^[13]

Schmidt and Gross^[14] use a boundary integral technique to perform the energy minimization in order to determine the equilibrium precipitate shapes in an elastically inhomogeneous and anisotropic medium, which is also used for studying multi-particle interactions in Reference 15. As an extension, Schmidt *et al.*^[16] have determined the 3D equilibrium precipitate morphologies using a boundary integral method. They have observed that there is a strong influence of elastic inhomogeneity, elastic anisotropy, and characteristic length on the morphological stability of precipitates. Similarly, Jog *et al.*^[17,18] use a finite element method coupled with a congruent-gradient-based optimization technique to minimize the sum of elastic and interfacial energies to determine equilibrium precipitate shapes of isolated, coherent particles with cubic anisotropy in elastic energy. They have also estimated symmetry breaking as a function of particle size for different combinations of elastic anisotropies and misfits. Jou *et al.*^[19] use a boundary integral method to study single precipitate growth as well as two-precipitate interactions. Kolling *et al.*^[20] use a finite element and optimization-based method to predict the equilibrium precipitate shape for misfitting particles with dilatational eigenstrain. The authors show that the value of the elastic constant, particle size, and inhomogeneity affect the stability of equilibrium shape of precipitate. Akaiwa *et al.*^[21] utilize the boundary integral method with a fast multipole method for integration, in order to simulate growth and coarsening of large number of precipitates.

An interesting extension of the finite element-based method for the prediction of the equilibrium shape is the utilization of the level-set method where a prescribed value of the level-set surface is used to describe the interface morphology.^[22] The model is used for modeling solid-state dendrite growth as well as coarsening, by coupling with an evolution equation for the composition field. The modification of the modeling scheme for the study of equilibrium shapes of precipitates is done by using a Lagrange parameter which maintains the same volume of the precipitate while the normal velocities of the interfacial nodes are calculated.^[23] The equilibrium shape is determined when the velocity of all the interfacial nodes becomes zero. As an extension of the model, the authors also study chemo-mechanical equilibrium where the misfit strains are a function of the composition in Reference 24, and the authors solve for diffusional equilibrium along with the equations for mechanical equilibrium.

In terms of the determination of the equilibrium morphologies of precipitates, the preceding models are all sharp-interface-based methods and in addition prescribe optimization solutions for the shape of the equilibrium precipitate under the constraint of constant volume. A corresponding approach using a microstructural evolution-based method is proposed by Khachatryan and colleagues,^[25] wherein precipitate evolution is simulated using a modified version of the Cahn–Hilliard equation^[26] until there is a complete loss of saturation or the situation where the diffusion potential everywhere becomes the same. In this situation, the shape of the precipitate corresponds to equilibrium. However, there is no explicit volume constraint during evolution and the variation of the equilibrated shapes as a function of the sizes/volume of the precipitate may only be tracked through a corresponding change in the alloy composition, yielding different volume fractions of the precipitate in a box of given size. Using this model, the authors have studied the effect of elastic stresses on precipitate shape instability during growth of single precipitates embedded in an elastically anisotropic system. Similar models have also been formulated by Leo *et al.*,^[27] where the authors solve for diffusional equilibrium along with the constraint of mechanical equilibrium in order to determine the equilibrium particle shape. The authors also compare with the results from their corresponding boundary-integral-based modeling methods.^[19] The authors also highlight the advantage of using the diffuse-interface schemes where merging and splitting of particles can be handled easily in contrast to the sharp-interface methods which require re-meshing. A similar dynamic evolution model has also been used to predict equilibrium shapes in 3Ds in Reference 28. Apart from the determination of equilibrium shapes, the diffuse-interface methods have also been used for the study of growth and coarsening of multi-particle systems,^[27,29–34] instabilities,^[35] and rafting.^[36–41]

In all the above studies, the central focus of investigation has been the study of equilibrium shapes of precipitates where the anisotropy exists only in the elastic energy. The coupled influence of both the

interfacial energy and elastic anisotropies on the equilibrium morphologies is performed using the boundary integral method by Leo *et al.*^[42] In a study by Greenwood *et al.*,^[43] the authors have developed a phase-field model of microstructural evolution, where they study the morphological evolution of solid-state dendrites as function of anisotropies in both surface as well as elastic energy. While the study is not particularly aimed at the computation of equilibrium shapes, the authors illustrate transitions in the growth directions of solid-state dendrites from those dominated by the surface energy anisotropy to those along elastically soft directions, stimulated by a change in the relative strengths of the anisotropies.

This brings us to the motivation of our paper, wherein we formulate a diffuse-interface model for the determination of equilibrium shapes of precipitates under the combined influence of anisotropies in both elastic as well as interfacial energies, with any combination of misfits. Here, the shape of the precipitate will be defined by a smooth function, which varies from a fixed value in the bulk of the precipitate to another in the matrix. The shape of the precipitate will be described by a fixed contour line of this function. Our work can be seen as a diffuse-interface counterpart of previous work by Voorhees *et al.*^[10] and other sharp-interface models by Schmidt and Gross^[14] and Jog *et al.*^[17] as well as the level-set-based FEM method proposed by Dudu *et al.*^[22] and Zhao *et al.*^[23,24] Herein, we use a modification of the volume-preserved Allen–Cahn evolution equation that was proposed previously by Nestler and colleagues,^[44] wherein the Allen–Cahn equation prescribing the evolution of a given order parameter is modified such that the integrated change in the volume that is computed over the entire domain of integration returns zero. The motivation for proposing a diffuse-interface model is threefold: firstly given that the Allen–Cahn dynamics for the order parameter ensures energy minimization, there is no requirement for an additional optimization routine that is used in corresponding works by Schmidt and Gross^[14] and Jog *et al.*^[17] Secondly, complicated discretization and solution routines adopted in Reference 10 can be avoided allowing for an easy extension from two dimensions (2Ds) to 3Ds. Thirdly, a diffuse-interface approach allows for an easy coupling of elastic and surface energy anisotropies. Further, a corollary to the ease of discretization is that quite complicated shapes with rapid change in curvatures can be treated with a great deal of accuracy, which we will demonstrate by comparing our results with those from a sharp-interface model. Additionally, our diffuse-interface presentation will be different from the previous phase-field models where we do not solve for the composition field while deriving the equilibrium shape of the precipitate which allows us to reduce the computational effort.

In the following sections, we firstly describe the model, followed by a discussion on the results which include benchmarks with analytical as well as with a previous FEM-based model by Jog *et al.*^[17] We then continue with other combinations of tetragonal misfits and elastic anisotropies, finally concluding with a study

involving a competition between elastic and interfacial energy anisotropy and its influence on equilibrium shapes. We conclude, with comparative statements between the different approaches and possible extensions of the model for investigations in multi-component systems.

II. MODEL FORMULATION

During solid-state phase transformations, a difference of the lattice parameter between the precipitate and the matrix gives rise to misfit strains/stresses for a coherent interface. This in turn contributes to the system energy in terms of an elastic contribution which scales with the volume of the precipitate. Similarly, the interfacial energy which is the other component of the energy in the system, varies with the interfacial area. In this context, the equilibrium shape of the precipitate is the one which minimizes the sum total of the contributions from both the elastic energy and interfacial components, which given the scaling of the two energy components is a function of the size of the precipitate.

In this section, we formulate a phase-field model, where the functional consists of both the elastic and the interfacial energy contributions. Since the equilibrium precipitate shape depends on the size of the precipitate, we formulate a model which minimizes the system energy while preserving the volume of the precipitate, and thereby allows the computation of the equilibrium shape of precipitates. This allows the determination of the precipitate shapes as a function of the different precipitate sizes as has been done previously using sharp-interface methods. This constrained minimization is achieved through the technique of volume preservation which is also described elsewhere^[44] that is essentially the coupling of the Allen–Cahn type equation with a correction term using a Lagrange parameter that ensures the conservation of the precipitate volume during evolution.

In the following, we discuss the details of the phase-field model. We begin with the free energy functional that reads

$$\mathcal{F}(\phi) = \int_V \left[\gamma W a^2(\mathbf{n}) |\nabla \phi|^2 + \frac{1}{W} w(\phi) \right] dV + \int_V f_{\text{el}}(\mathbf{u}, \phi) dV + \lambda_\beta \int_V h(\phi) dV, \quad [1]$$

where V is the total volume of system. ϕ is the phase-field order parameter that describes the presence and absence of precipitate (α phase) $\phi = 1$ and matrix (β phase) $\phi = 0$ phases. The first integral constitutes the interfacial energy contribution, which in a phase-field formulation is done using a combination of the gradient-energy and potential contributions. Here, the term γ controls the interfacial energy in the system, while W influences the width of the diffuse interface separating the precipitate and the matrix phases. The function $a(\mathbf{n})$ which is a function of the interface normal $\mathbf{n} = -\frac{\nabla \phi}{|\nabla \phi|}$, describes the interfacial energy anisotropy of

the precipitate/matrix interface. The second term in the first integral describes the double obstacle potential, which writes as

$$w(\phi) = \frac{16}{\pi^2} \gamma \phi(1 - \phi) \quad \phi \in [0, 1], \quad [2]$$

$$= \infty \quad \text{otherwise.}$$

The second integral enumerates the elastic energy contribution to the free energy density of the system which is a function of the order parameter ϕ that is also used to interpolate between the phase properties and the misfit. λ_β is the Lagrange parameter that is added in order that the volume of the precipitate represented by the integral $\int_V h(\phi) dV$, where $h(\phi) = \phi^2(3 - 2\phi)$ is an interpolation polynomial that smoothly varies from 0 to 1, is conserved. The evolution of the order parameter ϕ is derived using the classical Allen–Cahn dynamics that writes as

$$\tau W \frac{\partial \phi}{\partial t} = - \frac{\delta F}{\delta \phi}, \quad [3]$$

and elaborates as

$$\tau W \frac{\partial \phi}{\partial t} = 2\gamma W \nabla \cdot \left[a(\mathbf{n}) \left[\frac{\partial a(\mathbf{n})}{\partial \nabla \phi} |\nabla \phi|^2 + a(\mathbf{n}) \nabla \phi \right] \right] \quad [4]$$

$$- \frac{16}{\pi^2} \frac{\gamma}{W} (1 - 2\phi) - \frac{\partial f_{\text{el}}(\mathbf{u}, \phi)}{\partial \phi} - \lambda_\beta h'(\phi),$$

where τ is the interface relaxation constant, which in the present modeling context is chosen as the smallest value that allows for a stable explicit temporal evolution using a simple finite difference implementation of the forward Euler-scheme. Note, ' denotes differentiation of the function with respect to its argument. In order to complete the energetic description, it is important to elaborate the elastic energy density $f_{\text{el}}(\mathbf{u}, \phi)$ in terms of the physical properties of the matrix and the precipitate phases that are the stiffness matrices, as well as the misfit. Here, we adopt two ways of interpolating the phase properties, one of them bearing similarity to the Khachaturyan scheme^[45] of interpolation and the other which is a tensorial interpolation which is elaborately described in Reference 46.

A. Khachaturyan Interpolation

In this interpolation method, the elastic energy density writes as

$$f_{\text{el}}(\mathbf{u}, \phi) = \frac{1}{2} C_{ijkl}(\phi) (\epsilon_{ij} - \epsilon_{ij}^*(\phi)) (\epsilon_{kl} - \epsilon_{kl}^*(\phi)), \quad [5]$$

where the total strain can be computed from the displacement \mathbf{u} as

$$\epsilon_{ij} = \frac{1}{2} \left(\frac{\partial u_i}{\partial x_j} + \frac{\partial u_j}{\partial x_i} \right), \quad [6]$$

while the elastic constants C_{ijkl} and eigenstrain ϵ_{ij}^* can be expressed as follows:

$$C_{ijkl}(\phi) = C_{ijkl}^\alpha \phi + C_{ijkl}^\beta (1 - \phi), \quad [7]$$

$$\epsilon_{ij}^*(\phi) = \epsilon_{ij}^{*\alpha} \phi + \epsilon_{ij}^{*\beta} (1 - \phi).$$

To simplify the equations, without any loss of generality, we additionally impose that the eigenstrain exists only in precipitate phase (α phase), which makes $\epsilon_{ij}^{*\beta} = 0$. Thereafter, the elastic energy density can be recast as

$$f_{\text{el}}(\phi) = Z_3(\phi)^3 + Z_2(\phi)^2 + Z_1\phi + Z_0, \quad [8]$$

where, in Eq. [8], we segregate the terms in powers of ϕ , i.e., Z_3, Z_2, Z_1, Z_0 . Each pre-factor is a polynomial of ϕ , elastic constants and the misfit strains. The expansion of these pre-factors is illustrated in Appendix. Therefore, the term corresponding to the elastic energy in the evolution equation of the order parameter can be computed as

$$\frac{\partial f_{\text{el}}(\mathbf{u}, \phi)}{\partial \phi} = 3Z_3(\phi)^2 + 2Z_2(\phi) + Z_1. \quad [9]$$

B. Tensorial Interpolation

In this subsection, we utilize an interpolation scheme which allows the stress/strain terms normal and tangential to the phase-interface to be interpolated differently. An elaborate description for the motivation behind this can be found in References 46,47. Concisely, this allows for an efficient control on the excess energy at the interface that in principle should enable an easier comparison with analytical models. We elaborate the scheme for 2Ds, but in principle can also be generalized for more than 2Ds.

In this interpolation scheme, we rotate the stiffness tensors which are prescribed in the Cartesian coordinate system into the system that is described by the local unit normal vector and the tangent of the α/β interface. This is done using the unit normal vector of the interface,

$$\mathbf{n} = - \frac{\nabla \phi}{|\nabla \phi|}. \quad [10]$$

Describing a transformation from the Cartesian system \mathbf{x}, \mathbf{y} to \mathbf{n}, \mathbf{t} where after rotation of \mathbf{x} matches \mathbf{n} and \mathbf{t} matches \mathbf{y} , the transformation of stiffness tensor can be written as follows:

$$C_{nrts} = a_{ni} a_{tj} a_{rk} a_{sl} C_{ijkl}. \quad [11]$$

Similarly, the transformation of stress and strain tensor (including the eigenstrain tensor) can be written as follows:

$$\begin{aligned}\sigma_{nn} &= a_{nx}a_{nx}\sigma_{xx}, & \sigma_{nt} &= a_{nx}a_{ty}\sigma_{xy}, \\ \epsilon_{nn} &= a_{nx}a_{nx}\epsilon_{xx}, & \epsilon_{nt} &= a_{nx}a_{ty}\epsilon_{xy},\end{aligned}\quad [12]$$

where the transformation matrix can be expressed using rotation matrix, where we elaborate each element of rotation matrix as follows:

$$\begin{aligned}a_{xn} &= \cos\left(\tan^{-1}\frac{n_x}{n_y}\right) = a_{nx}, \\ a_{xt} &= -\sin\left(\tan^{-1}\frac{n_x}{n_y}\right) = a_{tx}, \\ a_{yn} &= \sin\left(\tan^{-1}\frac{n_x}{n_y}\right) = a_{ny}, \\ a_{yt} &= -\cos\left(\tan^{-1}\frac{n_x}{n_y}\right) = a_{ty}.\end{aligned}$$

The elastic energy of each of the phases writes as

$$f_{el} = \frac{1}{2}\sigma_{ij}(\epsilon_{ij} - \epsilon_{ij}^*), \quad [13]$$

which can be further elaborated for the transformed coordinate system, where we express the elastic energy in terms of normal and tangential components of stresses and strains as

$$f_{el} = \frac{1}{2}(\sigma_{nn}(\epsilon_{nn} - \epsilon_{nn}^*) + 2\sigma_{nt}(\epsilon_{nt} - \epsilon_{nt}^*) + \sigma_{tt}(\epsilon_{tt} - \epsilon_{tt}^*)). \quad [14]$$

The interpolated elastic energy can then be described as

$$\begin{aligned}f_{el}(\mathbf{u}, \phi) &= f_{el}^\alpha(\epsilon_{nn}^\alpha(\mathbf{u}, \phi), \epsilon_{nt}^\alpha(\mathbf{u}, \phi), \epsilon_{tt}^\alpha)h(\phi) \\ &+ f_{el}^\beta(\epsilon_{nn}^\beta(\mathbf{u}, \phi), \epsilon_{nt}^\beta(\mathbf{u}, \phi), \epsilon_{tt}^\beta)(1 - h(\phi)).\end{aligned}\quad [15]$$

Note, the usage of the superscripts on some of the terms, ϵ_{nn} , ϵ_{nt} , σ_{tt} , while the others ϵ_{tt} , σ_{nn} , σ_{nt} are left free, which is related to the jump conditions at the interface. In this interpolation scheme, the normal stress components σ_{nn} , σ_{nt} and ϵ_{tt} are continuous variables across the interface, which are derived from the condition of continuity of normal tractions at the interface (in the absence of interfacial stresses) and the Hadamard boundary conditions^[48] respectively, while the others ϵ_{nn} , ϵ_{nt} , σ_{tt} have a discontinuity in the sharp-interface free-boundary problem, which would translate to a smooth variation across the interface in the diffuse interface description. In order to affect this idea, the following scheme for the determination of the stress and strain components is adopted.

Firstly, the individual normal stress components of each of the phases are written down explicitly as a function of the stiffness and the strains as

$$\begin{aligned}\sigma_{nn} &= C_{nntt}^{\alpha,\beta}(\epsilon_{tt} - \epsilon_{tt}^{*\alpha,\beta}) + C_{nnnn}^{\alpha,\beta}(\epsilon_{nn}^{\alpha,\beta} - \epsilon_{nn}^{*\alpha,\beta}) \\ &+ 2C_{nnnt}^{\alpha,\beta}(\epsilon_{nt}^{\alpha,\beta} - \epsilon_{nt}^{*\alpha,\beta}), \\ \sigma_{nt} &= C_{nttt}^{\alpha,\beta}(\epsilon_{tt} - \epsilon_{tt}^{*\alpha,\beta}) + C_{ntnn}^{\alpha,\beta}(\epsilon_{nn}^{\alpha,\beta} - \epsilon_{nn}^{*\alpha,\beta}) \\ &+ 2C_{ntnt}^{\alpha,\beta}(\epsilon_{nt}^{\alpha,\beta} - \epsilon_{nt}^{*\alpha,\beta}),\end{aligned}\quad [16]$$

where ϵ^* is the eigenstrain at the interface produced due to a lattice mismatch between the precipitate and matrix. As mentioned before, we will be assuming that the eigenstrain is accommodated in the α phase, such that the eigenstrain in the β phase is zero. After some re-arrangement, the individual non-homogeneous normal strain-fields in either phase can be written as functions of the continuous variables which are the normal stresses and the tangential strain as

$$\begin{bmatrix} \epsilon_{nn}^{\alpha,\beta} - \epsilon_{nn}^{*\alpha,\beta} \\ \epsilon_{nt}^{\alpha,\beta} - \epsilon_{nt}^{*\alpha,\beta} \end{bmatrix} = \begin{bmatrix} C_{nnnn}^\alpha & 2C_{nnnt}^\alpha \\ C_{ntnn}^\alpha & 2C_{ntnt}^\alpha \end{bmatrix}^{-1} \begin{bmatrix} \sigma_{nn} - C_{nntt}^\alpha(\epsilon_{tt} - \epsilon_{tt}^{*\alpha}) \\ \sigma_{nt} - C_{nttt}^\alpha(\epsilon_{tt} - \epsilon_{tt}^{*\alpha}) \end{bmatrix}. \quad [17]$$

Similarly, for matrix phase, where there is no eigenstrain, the phase normal strains read

$$\begin{bmatrix} \epsilon_{nn}^\beta \\ \epsilon_{nt}^\beta \end{bmatrix} = \begin{bmatrix} C_{nnnn}^\beta & 2C_{nnnt}^\beta \\ C_{ntnn}^\beta & 2C_{ntnt}^\beta \end{bmatrix}^{-1} \begin{bmatrix} \sigma_{nn} - C_{nntt}^\beta\epsilon_{tt} \\ \sigma_{nt} - C_{nttt}^\beta\epsilon_{tt} \end{bmatrix}. \quad [18]$$

In order to have a smooth variation of non-homogeneous variables, we impose the following interpolation upon the individual strain components as

$$\begin{bmatrix} \epsilon_{nn} \\ \epsilon_{nt} \end{bmatrix} = \begin{bmatrix} \epsilon_{nn}^\alpha \\ \epsilon_{nt}^\alpha \end{bmatrix}h(\phi) + \begin{bmatrix} \epsilon_{nn}^\beta \\ \epsilon_{nt}^\beta \end{bmatrix}(1 - h(\phi)). \quad [19]$$

Expressing the inverse matrices in the previous relations as S_{nt}^α and S_{nt}^β for the respective phases and further simplifying for the stress tensor σ_{nn} and σ_{nt} we can derive

$$\begin{aligned}\begin{bmatrix} \sigma_{nn} \\ \sigma_{nt} \end{bmatrix} &= \left(S_{nt}^\alpha h(\phi) + S_{nt}^\beta (1 - h(\phi)) \right) \\ &\left\{ \begin{bmatrix} \epsilon_{nn} - \epsilon_{nn}^{*\alpha} h(\phi) \\ \epsilon_{nt} - \epsilon_{nt}^{*\alpha} h(\phi) \end{bmatrix} + S_{nt}^\alpha \begin{bmatrix} C_{nntt}^\alpha(\epsilon_{tt} - \epsilon_{tt}^{*\alpha}) \\ C_{nttt}^\alpha(\epsilon_{tt} - \epsilon_{tt}^{*\alpha}) \end{bmatrix} h(\phi) \right. \\ &\left. + S_{nt}^\beta \begin{bmatrix} C_{nntt}^\beta\epsilon_{tt} \\ C_{nttt}^\beta\epsilon_{tt} \end{bmatrix} (1 - h(\phi)) \right\},\end{aligned}\quad [20]$$

where the local strains ϵ_{nn} , ϵ_{tt} , ϵ_{nt} can be derived from the displacement using Eq. [6] followed by a coordinate transformation to the \mathbf{n} , \mathbf{t} space. Thus, we can derive the values of $\epsilon_{nn}^{\alpha,\beta}$ and $\epsilon_{nt}^{\alpha,\beta}$ by inserting above relation in previous strain calculations, *i.e.*, Eqs. [17] and [18].

The remaining stress component σ_{tt} , *i.e.*, the tangential component of stress is also non-homogeneous and can be derived by firstly imposing a smooth interpolation across the diffuse interface, *i.e.*,

$$\sigma_{tt} = \sigma_{tt}^\alpha h(\phi) + \sigma_{tt}^\beta (1 - h(\phi)), \quad [21]$$

where each of the phase stress components $\sigma_{tt}^{\alpha,\beta}$ can be written as a function of the normal strain components that have already been derived and the continuous tangential strain component that is just a function of the local displacement.

Therefore, relations for σ_{tt}^α and σ_{tt}^β write as

$$\sigma_{tt}^\alpha = C_{ttnn}^\alpha (\epsilon_{nn}^\alpha - \epsilon_{nn}^{*\alpha}) + 2C_{ttnt}^\alpha (\epsilon_{nt}^\alpha - \epsilon_{nt}^{*\alpha}) + C_{tttt}^\alpha (\epsilon_{tt} - \epsilon_{tt}^{*\alpha}), \quad [22]$$

$$\sigma_{tt}^\beta = C_{ttnn}^\beta \epsilon_{nn}^\beta + 2C_{ttnt}^\beta \epsilon_{nt}^\beta + C_{tttt}^\beta \epsilon_{tt}. \quad [23]$$

Since the values of $\epsilon_{nn}^{\alpha,\beta}$, $\epsilon_{nt}^{\alpha,\beta}$ are already determined in terms of ϵ_{nn} , ϵ_{nt} and ϵ_{tt} , the value of $\sigma_{tt}^{\alpha,\beta}$ can be solved using preceding relations. Inserting them into equation for σ_{tt} , helps to determine the final stress component as function of strains.

In this event, the variational derivative of elastic energy of the system at constant stress, strain, and displacement can be derived from Eq. [15] as

$$\begin{aligned} \left(\frac{\partial f_{el}}{\partial \phi}\right)_{\sigma,\epsilon,u} &= (f_{el}^\alpha - f_{el}^\beta) \frac{\partial h(\phi)}{\partial \phi} + \sum_\alpha \frac{\partial f_{el}^\alpha}{\partial \epsilon_{nn}^\alpha} \frac{\partial \epsilon_{nn}^\alpha}{\partial \phi} h_\alpha(\phi) \\ &+ 2 \sum_\alpha \frac{\partial f_{el}^\alpha}{\partial \epsilon_{nt}^\alpha} \frac{\partial \epsilon_{nt}^\alpha}{\partial \phi} h_\alpha(\phi), \end{aligned} \quad [24]$$

where for conciseness we introduce the notation $h_\alpha(\phi) = h(\phi)$ and $h_\beta(\phi) = 1 - h(\phi)$, and summations on the RHS, run over the phases, α, β . The derivative with respect to the variable ϵ_{tt} returns zero, as it is a homogeneous quantity. In order to determine the derivative of non-homogeneous variables, we utilize Eq. [19]. Differentiating Eq. [19] at constant displacement and strain gives us the following relations:

$$\begin{bmatrix} -\epsilon_{nn}^\alpha - \epsilon_{nn}^\beta \\ \epsilon_{nt}^\alpha - \epsilon_{nt}^\beta \end{bmatrix} \frac{\partial h_\alpha(\phi)}{\partial \phi} = \sum_\alpha \begin{bmatrix} \frac{\partial \epsilon_{nn}^\alpha}{\partial \phi} \\ \frac{\partial \epsilon_{nt}^\alpha}{\partial \phi} \end{bmatrix} h_\alpha(\phi). \quad [25]$$

Also recall that

$$\frac{\partial f_{el}^{\alpha,\beta}}{\partial \epsilon_{nn}^{\alpha,\beta}} = \sigma_{nn}, \quad \frac{\partial f_{el}^{\alpha,\beta}}{\partial \epsilon_{nt}^{\alpha,\beta}} = \sigma_{nt}, \quad [26]$$

which follow from the definition of the elastic energy.

Substituting these values and rewriting the variational derivative, we derive

$$\begin{aligned} \left(\frac{\partial f_{el}}{\partial \phi}\right) &= (f_{el}^\alpha - f_{el}^\beta - \sigma_{nn}(\epsilon_{nn}^\alpha - \epsilon_{nn}^\beta)) \frac{\partial h(\phi)}{\partial \phi} \\ &- 2\sigma_{nt}(\epsilon_{nt}^\alpha - \epsilon_{nt}^\beta) \frac{\partial h(\phi)}{\partial \phi}. \end{aligned} \quad [27]$$

This relation can be simplified further by substituting the values for f_{el}^α and f_{el}^β explicitly in terms of the stresses and the strains as

$$\begin{aligned} \left(\frac{\partial f_{el}(\mathbf{u}, \phi)}{\partial \phi}\right) &= \left[-\frac{1}{2} \sigma_{nn}(\epsilon_{nn}^\alpha - \epsilon_{nn}^\beta) - \sigma_{nt}(\epsilon_{nt}^\alpha - \epsilon_{nt}^\beta) \right. \\ &- \frac{1}{2} \sigma_{tt}^\alpha \epsilon_{tt}^{*\alpha} - \frac{1}{2} \sigma_{nn} \epsilon_{nn}^{*\alpha} - \sigma_{nt} \epsilon_{nt}^{*\alpha} \\ &\left. + \frac{1}{2} (\sigma_{tt}^\alpha - \sigma_{tt}^\beta) \epsilon_{tt} \right] \frac{\partial h(\phi)}{\partial \phi}. \end{aligned} \quad [28]$$

C. Conservation of Volume

The remaining part of the evolution equation [4] that is yet to be determined is the Lagrange parameter λ_β which would conserve the volume during interface evolution. Volume conservation is affected through the constraint,

$$\int h(\phi) \cdot dx = \text{const} \quad \text{or} \quad [29]$$

$$\int \delta h(\phi) dx = 0, \quad [30]$$

where $\delta h(\phi)$ is the change in the value of $h(\phi)$ at a given spatial location. Reformulation of this condition in discrete terms is performed in the following manner. From Eq. [4], we have the rate of change of the order parameter at a given location, *i.e.*,

$$\tau W \frac{\partial \phi}{\partial t} = \text{rhs}_x - \lambda_\beta h'(\phi), \quad [31]$$

where the term rhs_x constitutes all the terms in the evolution equation of the order parameter in Eq. [4] leaving out the Lagrange parameter. In order to affect the volume constraint as given by Eq. [29], the Lagrange parameter λ_β is computed as

$$\lambda_\beta = \frac{\sum_V \text{rhs}_x}{\sum_V h'(\phi)}, \quad [32]$$

where the summation \sum_V is over the entire volume. This essentially ensures that the summation of all the changes in the order parameter over the entire volume returns zero, thus affecting the volume constraint in the discrete framework.

D. Mechanical Equilibrium

As a final aspect, what remains is the computation of the displacement fields as a function of the spatial distribution of the order parameter. This is done iteratively by solving the damped wave equation written as

$$\rho \frac{d^2 \mathbf{u}}{dt^2} + b \frac{d\mathbf{u}}{dt} = \nabla \cdot \boldsymbol{\sigma}, \quad [33]$$

that is solved until the equilibrium is reached, *i.e.*, $\nabla \cdot \boldsymbol{\sigma} = \mathbf{0}$. The terms ρ and b are chosen such that the

convergence is achieved in the fastest possible time. The computation of the stresses differs depending upon the interpolation schemes used for estimating the elastic energies. For the case of the Khachaturyan interpolation, the stresses at every point can be readily computed as a partial derivative of the elastic energy as $\sigma_{ij} = \frac{\partial f_{el}(\mathbf{u}, \phi)}{\partial \epsilon_{ij}}$, while for the tensorial interpolation, the estimation of the stresses is done differently as laid out in the preceding section (see Section II–B).

The optimization procedure for finding the equilibrium shape is performed by solving the evolution of the order parameter ϕ in Eq. [4] along with the equation of mechanical equilibrium at each time step, until a converged shape is reached.

III. RESULTS

A. Model Parameters

In this section, we list out the material parameters and the non-dimensionalization scheme that will be used in the subsequent sections. Firstly, we will limit ourselves to isotropic and cubic systems in 2Ds, such that the stiffness tensor can be simplified. These systems can be generically defined in the following manner, where we use the commonly used short-hand notation for the non-zero stiffness components, $C_{11} = C_{1111}$, $C_{22} = C_{2222}$, $C_{12} = C_{1122}$ and $C_{44} = C_{1212}$, where additionally $C_{11} = C_{22}$ because of symmetry considerations. Thereafter, these terms can be derived in terms of the known material parameters, those are the Zener anisotropy (A_z), Poisson ratio (ν), and shear modulus (μ) and can be written as

$$C_{44} = \mu, \quad C_{12} = 2\nu \left(\frac{C_{44}}{1 - 2\nu} \right), \quad C_{11} = C_{12} + \frac{2C_{44}}{A_z}. \quad [34]$$

The eigenstrain matrix will be considered diagonal in the Cartesian coordinate system and reads

$$\epsilon^* = \begin{bmatrix} \epsilon_{xx}^* & 0 \\ 0 & \epsilon_{yy}^* \end{bmatrix}. \quad [35]$$

We use a non-dimensionalization scheme where the energy scale is set by the interfacial energy scale 1.0 J/m^2 divided by the scale of the shear modulus $1 \times 10^9 \text{ J/m}^3$ that yields a length scale $l^* = 1 \text{ nm}$. In the paper, hence all the parameters will be reported in the terms of non-dimensional units. Unless otherwise specified, all results are produced with $\mu_{\text{mat}} = 125$, $\nu_{\text{ppt}} = \nu_{\text{mat}} = 0.3$ and A_z varies from 0.3 to 3.0. When $A_z = 1.0$, elastic constants become isotropic. When A_z is greater than unity, elastically soft directions are $\langle 100 \rangle$, whereas elastically hard directions are $\langle 110 \rangle$. Similarly, in the case where A_z is less than unity, elastically soft (hard) directions are $\langle 110 \rangle$ ($\langle 100 \rangle$). For all the cases, the precipitate and matrix have the same magnitude of A_z .

The diagonal components of misfit strain tensor are assumed to be aligned along $\langle 100 \rangle$ directions in (001)

plane of the cubic system, whereas the off-diagonal terms are zero. The misfit strain or eigenstrain (ϵ^*) can be dilatational, *i.e.*, the same along principle directions ($\epsilon_{xx}^* = \epsilon_{yy}^*$) or tetragonal, *i.e.*, different along principle directions ($\epsilon_{xx}^* \neq \epsilon_{yy}^*$). For different cases, the magnitude of eigenstrain varies from 0.5 to 2 pct.

For all our simulations, we have utilized a two-dimensional system of a precipitate embedded in a matrix, with a lattice mismatch at the interface that is coherent. Domain boundaries follow periodic conditions. The ratio of the initialized precipitate size (equivalent radius) to the matrix size is maintained as 0.08, such that there is a negligible interaction of the displacement field at the boundaries for the prescribed ratio. This resembles the condition of an infinitely large matrix containing an isolated precipitate without any influence of external stress. The interfacial energy between the matrix and precipitate is assumed to be isotropic until specified. The magnitude of interfacial energy is considered to be 0.15.

The model is generic enough for incorporating any combination of anisotropies in elastic energy which are possible in two dimensional space. In addition, different stiffness values in the phases can also be modeled. In our model formulation, we will use the ratio of the shear moduli δ in order to characterize the degree of inhomogeneity, wherein a softer precipitate is derived by a value of δ that is less than unity, and *vice versa* for the case of a harder precipitate.

B. Isotropic Elastic Energy

As the first case, we consider isotropic elastic moduli ($A_z = 1.0$) with dilatational misfit at the interface between precipitate and matrix ($\epsilon_{xx}^* = \epsilon_{yy}^* = 0.01$). For this case, we consider the precipitate to be softer than matrix, *i.e.*, the inhomogeneity ratio, $\delta = 0.5$.

We begin the simulation with an arbitrary shape as an initial state of precipitate, *e.g.*, an ellipse with an arbitrary aspect ratio, that is the ratio of the lengths of the major and the minor axes. We formulate a shape factor in terms of the major axis (c) and minor axis (a), which is expressed as $\rho = \frac{c-a}{c+a}$, that parameterizes the possible equilibrium shapes. An exemplary simulation showing the influence of the size is shown in Figure 1, where a precipitate with equivalent radius $R = 38$ (the radius of an equivalent circle of equivalent area) has a circular shape. With increase in the size of precipitate, the precipitate transforms to an elliptical shape, which is captured in Figure 1, where a precipitate with larger size, *i.e.*, equivalent radius, $R = 48$, acquires an ellipse-like configuration as the equilibrium shape.

This phenomenon has been theoretically studied by Johnson and Cahn,^[9] which they term as a symmetry breaking transition of a misfitting precipitate in an elastically stretched matrix. The shape transition from a circular to an ellipse-like shape can be presented distinctly by plotting the shape factor as a function of the characteristic length. The characteristic length is defined as ratio of characteristic elastic energy to interfacial energy which can be written as follows:

$$L = \frac{R\mu_{\text{mat}}\epsilon^{*2}}{\gamma}, \quad [36]$$

where R is the radius of a circular precipitate of equivalent area and γ is the magnitude of surface energy. Here, we briefly describe the Johnson–Cahn theory for shape bifurcation of a cylindrical precipitate. The solution for an elastically induced shape bifurcation of an inclusion can be derived, only when the precipitate is softer than a matrix. To do so, we express surface energy (f_s) and elastic energy (f_{el}) in terms of the area of the precipitate (A) and shape factor (ρ).

Thus, the total surface energy can be expressed as a Taylor series expansion in terms of ρ ,

$$f_s = 2\sigma\sqrt{\pi A} \left(1 + \frac{3}{4}\rho^2 + \frac{33}{64}\rho^4 + \dots \right). \quad [37]$$

In the same way, we express total elastic energy as

$$f_{\text{el}} = \frac{2A\epsilon^{*2}\mu_{\text{ppt}}}{1 + \delta - 2\nu_{\text{ppt}}} \left\{ 1 - \frac{\delta(1 - \delta)(1 + \kappa)}{(1 + \kappa\delta)(1 + \delta - 2\nu_{\text{ppt}})}\rho^2 + \frac{\delta(1 - \delta)^2(1 + \kappa)}{(1 + \kappa\delta)^2(1 + \delta - 2\nu_{\text{ppt}})^2}\rho^4 + \dots \right\}, \quad [38]$$

where ϵ^* is misfit at interface, $\delta = \mu_{\text{ppt}}/\mu_{\text{mat}}$ and $\kappa = 3 - 4\nu$.

The total energy (F^T) is the sum of f_s and f_{el} . Shape bifurcation takes place when the precipitate acquires a critical area A_c at which the energy landscape that is plotted as a function of the shape factor has distinct minima corresponding to the bifurcated shapes. This is akin to the example of classical spinodal decomposition where the compositions of the phases bifurcate below a critical temperature. Therefore, the critical size and the bifurcated shapes beyond it can be derived using the same common tangent construction as in spinodal decomposition, with the shape factor being used

similarly as the composition. Given the symmetry of the isotropic system, this equilibrium condition simplifies to

$$\frac{dF^T}{d\rho} = 0. \quad [39]$$

In this way, we take derivatives of the coefficients of the Taylor series from Eqs. [37] and [38] w.r.t. shape factor (ρ), and add the respective terms to solve for Eq. [39] as

$$\rho^3 \underbrace{3\sigma\sqrt{\pi A_c} f_s^1}_d - \underbrace{\frac{4A\epsilon^{*2}\mu^*\delta(1 - \delta)(1 + \kappa)}{(1 + \kappa\delta)(1 + \delta - 2\nu^*)^2} f_{\text{el}}^1}_d + \rho^3 \underbrace{\frac{33}{8}\sigma\sqrt{\pi A_c} f_s^2}_d + \underbrace{\frac{8\delta(1 - \delta)^2(1 + \kappa)A_c\epsilon^{*2}\mu^*}{(1 + \kappa\delta)^2(1 + \delta - 2\nu^*)^4} f_{\text{el}}^2}_d = 0. \quad [40]$$

By rearranging the terms, we get a stable solution for ρ that reads

$$\rho = \pm \sqrt{\frac{df_{\text{el}}^1 - df_s^1}{df_s^2 + df_{\text{el}}^2}}. \quad [41]$$

By substituting for the variables in Eq. [41], we plot the shape factors corresponding to the equilibrium solution as a function of the characteristic length. This is shown in Figure 2, where the thick dark line represents the analytical solution obtained from Eq. [41]. Maxima or unstable solutions occur for $\rho = 0$ for all the characteristic lengths beyond critical value.

Before venturing into a critical comparison between analytical and the phase-field results, it is important to ensure the numerical accuracy with respect to the choice of the parameters particularly the choice of the interface

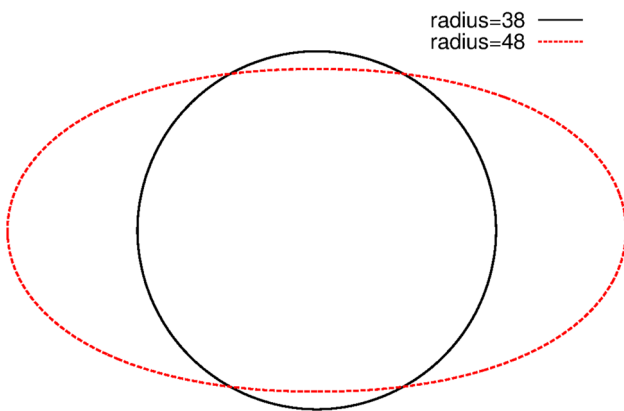


Fig. 1—Equilibrium shapes of precipitate with $R = 38$ ($L = 3.16$, thick line) and $R = 48$ ($L = 4.0$, dotted line), with $\delta = 0.5$, $\mu_{\text{mat}} = 125$, $\epsilon^* = 0.01$.

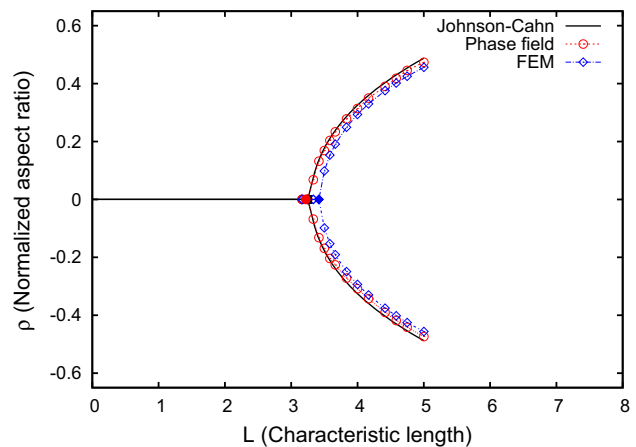


Fig. 2—Plot depicts the shape bifurcation diagram: comparison of analytical solution ($L_c = 3.25$ with dark square) with phase-field ($L_c = 3.21$ with red circle) and FEM ($L_c = 3.42$ with blue diamond) results, $A_z = 1.0$, $\epsilon^* = 0.01$, $\delta = 0.5$ (Color figure online).

width in the phase-field simulations. In the phase-field model that is described, the parameter that defines the diffuse-interface width W is a degree of freedom which may be increased or decreased depending on the morphological and macroscopic length scales that are being modeled. This choice of the diffuse-interface width W is typically chosen in a range such that the quantities being derived from the simulation results remain invariant. So for example in the present scenario it would be the shape factor of the precipitate and its variation with the change in the interface widths allows us to determine the range of W in which the shape factor is relatively constant. We have performed this convergence test for both the interpolation methods (recall from the model formulation: Khachaturyan and the Tensorial) described above and the comparison is described in Figure 3.

We find that for both interpolation methods relative invariance with change in the value of the interface width is achieved for values of $W \leq 2$, ($W/R = 0.08$), while for values greater the variation is non-linear and changes rapidly. Therefore, we have chosen values of $W = 2$ for performing the comparison between the different numerical methods (FEM and phase-field) and analytical calculations. It is noteworthy that in general phase-field methods show this variation with the change in the interface widths because of variation in the equilibrium phase-field profile arising out of a contribution to the total effective interfacial excesses from the bulk energetic terms that scales with the interface width. The other reason for variation with W arises because of higher order corrections in the stress/strain profiles as a result of the imposition of an interface between the two bulk phases. Here, it is interesting that although the tensorial formulation is seemingly more correct with regard to the removal of the interfacial excess contribution^[46] to the interfacial energy, however, this leads to no advantage with respect to the choice of larger interfacial widths, in comparison to the Khachaturyan interpolation method. A possible reason for this is the nature of the macroscopic length scale which in this case

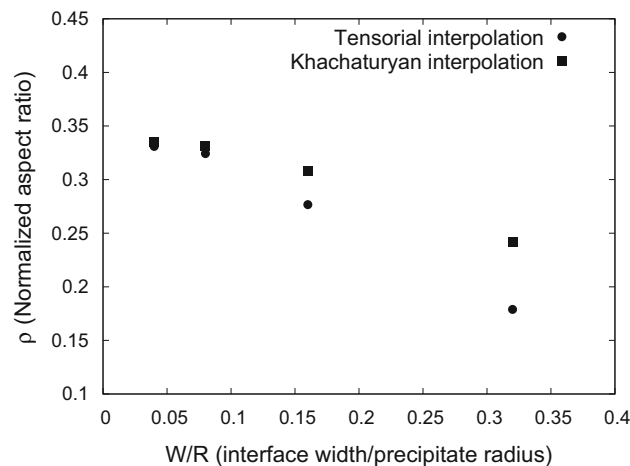


Fig. 3—Plot shows the variation of normalized aspect ratio (shape factor) as function of W/R , for $R = 25$, $A_z = 1.0$, $\epsilon^* = 0.01$, $\delta = 0.5$.

is the length over which the stress/strain profiles decay from the precipitate to the matrix that typically are proportional to the local radius of curvature of the precipitate. This implies that for smaller precipitates the decay is faster and occurs over a shorter length and *vice versa* for a larger precipitate. The accuracy of the phase-field method then will naturally depend on the ratio of the W/R which is applicable for both interpolation methods.

Given that the results of the variation of the shape factor for different interface widths for both interpolation methods, a seemingly qualitative conclusion that can be made is that it is ratio of the interface width w.r.t. to the macroscopic decay length of the stress/strain profiles and the error caused due to use of larger values leads to a more stringent condition for the choice of the interface widths than the errors arising from the contribution to the interfacial excesses due to incorrect interpolations of the stresses/strains at the interface. Therefore, given that the Khachaturyan method is numerically more efficient we have chosen this as the method in all our future simulation studies. The convergence test w.r.t. to the variations with the interface widths is repeated for the different bifurcation shapes both to verify and confirm the validity of the results as well as to perform the simulations in the most efficient manner by choosing the largest possible W with the admissible deviation in shape factor.

We now comment on the comparison between the different numerical and the analytical Johnson–Cahn theories with our phase-field results. We have obtained the normalized aspect ratio (ρ) and plotted it as a function of normalized precipitate size (characteristic length), from phase-field simulations. From Figure 2, it is evident that the precipitate has a circular shape ($\rho = 0$) below the critical point, and turns elliptical ($\rho \neq 0$) beyond it. Also, the transition from a circle to an ellipse-like shape is continuous, *i.e.*, ρ approaches zero, as L approaches a critical value L_c . It is evident from Figure 2 that phase-field results are in very good agreement with the analytical solution derived from the work of Johnson and Cahn,^[9] with a maximum error of 2.9 pct in the studied range of characteristic lengths. It is expected that deviations occur for larger characteristic lengths where the truncation errors in the analytical expressions to approximate the surface and the elastic energies start to become larger. Therefore, the phase-field results should be more accurate here.

Additionally, we compare our phase-field results with existing numerical methods, such as the model adopted by Jog *et al.*,^[17] where they used a sharp-interface, finite element method coupled with an optimization technique to determine the equilibrium shape of a coherent, misfitting precipitate. Using this method, we have reproduced the equilibrium shapes of precipitates, for the same set of conditions. It is clear that the results obtained from the sharp-interface FEM model follow similar trends as that of the phase-field results (Figure 2). Note that, the errors are larger near the critical point, which is expected to be better retrieved in the phase-field method, given its greater resolution of the shape and lesser grid-anisotropy. Similarly for larger

precipitate shapes where the curvatures of the precipitates become larger at certain locations, again the phase-field method should yield a better estimate. Nevertheless, all three methods agree pretty well.

The critical size of the precipitate at shape transition can be determined from analytical solution as well as phase-field simulations and FEM methods. The parameter L_c characterizing this critical radius is determined by first fitting a curve to the data points and thereafter computing the intersection point of the curve with the line ($\rho = 0$). Analytical equation gives $R_c = 39.57$ ($L_c = 3.25$), whereas the phase-field method yields $R_c = 38.53$ ($L_c = 3.21$) while the FEM yields $R_c = 41.785$ ($L_c = 3.42$). Thus, with these critical comparisons, we have benchmarked our phase-field model quantitatively with both the analytical solution and the sharp-interface model.

Moreover, the number of variants for bifurcated shape is infinite since all the directions in xy -plane are equivalent due to infinite fold rotation symmetry about the z -axis. We have confirmed this fact by starting the simulation with different orientations to the initial configurations, which equilibrate along different orientations but with the same bulk energy. Also, for precipitates possessing greater elastic moduli than that of the matrix, *i.e.*, $\delta > 1.0$, there is no bifurcation observed. This fact is also in agreement with the analytical solution, as there exists no real solution for cases where $\delta > 1.0$.

C. Cubic Anisotropy in Elastic Energy with Dilatational Misfit

Anisotropy in the elastic energy arises from the variation of elastic constants in different directions. This deviation from the elastic isotropy is reflected in the increase in the number of independent elastic constants. Here, we mainly consider cubic anisotropy in the elastic energy, as it is observed in several alloys while precipitation and growth.

As explained in the previous section, eventually it is important to determine the range of W , where the shape factor remains constant for the different magnitudes of interfacial width. Anisotropy in the elastic energy modifies the magnitude of elastic constants, thus changing stress/strain variation across the interface moving from the precipitate to matrix. As we have mentioned in the earlier section, we perform the W -convergence test, where the variations of shape factor with the interface width are plotted in Figure 4. The shape factor is calculated as the ratio of precipitate size measured along the horizontal axis to the vertical axis, *i.e.*, the size of precipitate along the elastically softer directions. There is not a significant variation in measured shape factor as a function of interfacial width, *i.e.*, in the given range of W , where the variation is weakly linear. But, as described in the earlier section, we choose an optimum value of $W = 4$ ($W/R = 0.16$) with which we can efficiently run the simulations with an acceptable deviation in the calculated shape factor (*i.e.*, an error of about 9 pct from the value obtained by extrapolating to the y -axis or the case of $W = 0$, that

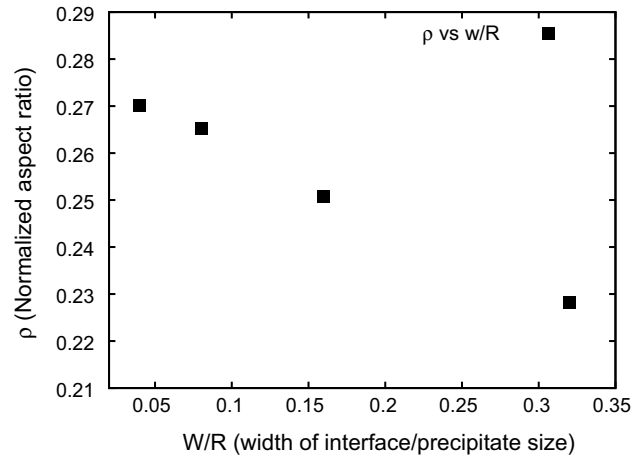


Fig. 4—The variation of normalized aspect ratio as a function of W/R , for $R = 25$, $A_z = 3.0$, $\epsilon^* = 0.01$, $\delta = 0.5$.

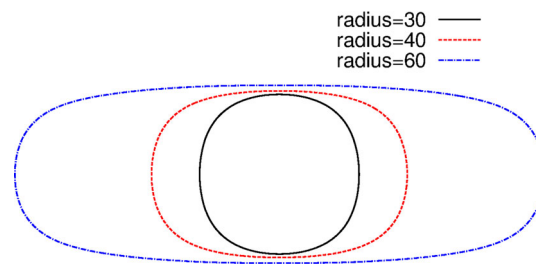


Fig. 5—Equilibrium shapes of precipitate with cubic anisotropy in elastic energy and with different sizes, $R = 30$ ($L = 2.5$), $R = 40$ ($L = 3.33$) and $R = 60$ ($L = 5$) for $A_z = 3.0$, $\epsilon^* = 0.01$, $\delta = 0.5$.

would effectively correspond to the sharp-interface limit).

Here, the elastic moduli possess cubic anisotropy while the misfit is dilatational. Thus, we have used $A_z = 3.0$, $\epsilon^* = 0.01$, $\delta = 0.5$, $\mu_{\text{mat}} = 125$. With these initial conditions, the phase-field simulations yield equilibrium precipitate morphologies as a function of the characteristic length, which are illustrated in Figure 5. Here, a precipitate with $R = 30$, acquires cubic (square-like) shape with rounded corners as an effect of cubic anisotropy in the elastic energy. The precipitate faces are normal to $\langle 100 \rangle$ directions, which are the elastically soft directions. In contrast to this, the precipitates with radii equal to 40 and 60 possess rectangular morphologies with rounded corners and elongated faces along one of the $\langle 100 \rangle$ directions. Depending upon the orientation of the initial configuration of the precipitate, *i.e.*, the elliptical shape for a given equivalent radius, it converges to two variants those are rectangle-like shapes, one aligned vertically (along $\langle 010 \rangle$ direction) whereas other along the horizontal axis (along $\langle 100 \rangle$ direction).

Upon a change in the anisotropy to a value lesser than unity, *i.e.*, $A_z = 0.3$, the equilibrium precipitate acquires a diamond like shape for $R = 40$, which is shown in Figure 6. With $A_z < 1$, the elastically softer directions now switch to $\langle 110 \rangle$ directions. This is evident from Figure 6, as the precipitate faces are oriented along $\langle 110 \rangle$ directions. Further, with increasing equivalent

radius of precipitate, the equilibrium shape loses its fourfold symmetry. The precipitate with increasing size tends to elongate along one of the elastically softer directions, *i.e.*, $\langle 110 \rangle$ directions. This is captured by giving a slight orientation to the starting configuration, where the precipitate eventually takes up a rectangle-like morphology (oriented along $\langle 110 \rangle$ direction), as shown in Figure 6.

The influence of precipitate size on the equilibrium morphologies of the precipitate can be quantified by plotting the normalized aspect ratio (shape factor, ρ) as a function of characteristic length (L) of the precipitate, as a bifurcation diagram. We evaluate such a bifurcation diagram for the case of $A_z = 3$. Figure 7 shows such a variation of the shape factor with respect to the

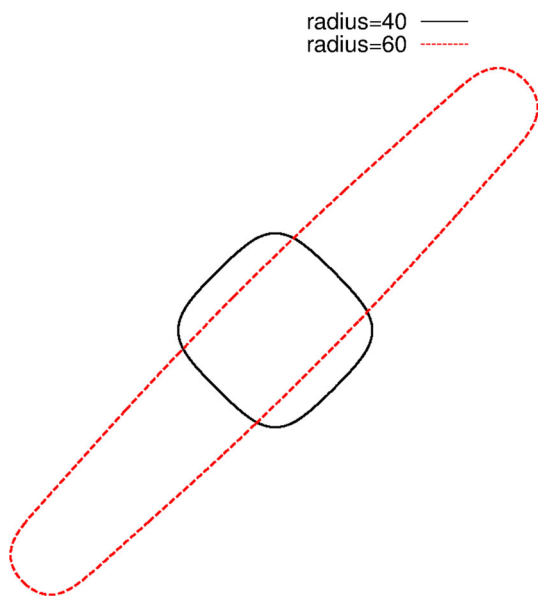


Fig. 6—Equilibrium shapes of precipitate with cubic anisotropy in elastic energy $R = 40$ ($L = 3.33$) and $R = 60$ ($L = 5$) for $A_z = 0.3$, $\epsilon^* = 0.01$, $\delta = 0.5$.

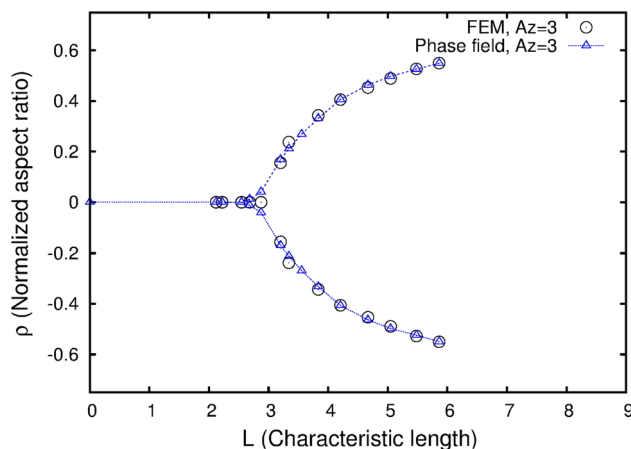


Fig. 7—The shape bifurcation diagram with cubic anisotropy in elastic energy ($A_z = 3.0$, $\epsilon^* = 0.01$, $\delta = 0.5$), where the variation of aspect ratio is plotted as function of characteristic length, a comparison of phase-field with FEM results.

precipitate size which reveals that the critical size for the bifurcation from cubic ($\rho = 0$) to the rectangle ($\rho \neq 0$) occurs for a value of $L = 2.71$.

As illustrated in the previous section, we have obtained the results for the equilibrium morphologies of the precipitate with cubic anisotropy in the elastic energy using a sharp-interface model (FEM), where the shape factor is calculated as a function of the characteristic length of the precipitate. This is shown in Figure 7, where the bifurcation diagram obtained from both the techniques, *i.e.*, phase-field as well as FEM are plotted against each other. It is evident that the bifurcation curves obtained from both simulation techniques agree well with each other. Both techniques predict the critical characteristic length (L_c), which are close to each other, *i.e.*, L_c retrieved from the phase-field simulation equals to 2.71, whereas the one obtained from FEM equals to 2.87. Far away from the bifurcation point, the normalized aspect ratios obtained from phase-field and FEM simulations predict nearly the same value, while near the bifurcation point (L_c) there is small variation, which is again expected as close to the critical point the resolution of the phase-field method should be better. In addition, the agreement between the two methods is also a critical additional benchmark of the phase-field model in the absence of an analytical solution predicting the shape factors for the case of cubic anisotropy.

D. Cubic Anisotropy in Elastic Energy with Tetragonal Misfit

1. Misfit components with same sign

In this subsection, we study the case of tetragonal misfit where the magnitude of eigenstrain is different along the principle directions but of the same sign, *i.e.*,

$$\epsilon^* = \begin{bmatrix} 0.01 & 0 \\ 0 & 0.005 \end{bmatrix}, \quad [42]$$

where we denote the misfit ratio with the parameter, $t = \epsilon_{xx}^*/\epsilon_{yy}^* = 2$. We consider three different cases, where the magnitude of A_z varies from 0.3 to 3.0, *i.e.*, $A_z < 1$, $A_z = 1$ and $A_z > 1$. Similar to the previous cases, here the initial configuration of the precipitate is considered as an ellipse with an arbitrary aspect ratio and orientation.

Figure 8 shows the equilibrium shapes of precipitate obtained with $A_z = 3.0$, for two different equivalent radii of precipitate ($R = 25, 50$). Here, the precipitate and matrix both possess the same elastic moduli, *i.e.*, $\delta = 1.0$. It is clear that the precipitate takes ellipse-like shape for the given sizes. The precipitate elongates along y -direction, *i.e.*, the direction along which the eigenstrain is lower. This implies that, with increase in the precipitate size, it will produce an equilibrium shape which aligns itself along the direction of smaller misfit while elongating along the same direction. Thus, for this situation, there is no shape bifurcation observed. Even for situations, where the magnitude of elastic anisotropy is $A_z \geq 1$ and $\delta \leq 1$, the precipitate morphologies remain ellipse like for the larger equivalent radii of precipitates.

In the succeeding condition, we consider $A_z = 0.3$ and $\delta = 1.0$ with the same tetragonality. The equilibrium morphologies for the smaller sizes are only moderately different than those observed in the previous case. Figure 9 illustrates the results with $A_z = 0.3$, where the precipitate size ranges from $R = 40$ to 65. The precipitate with comparatively smaller size takes up an

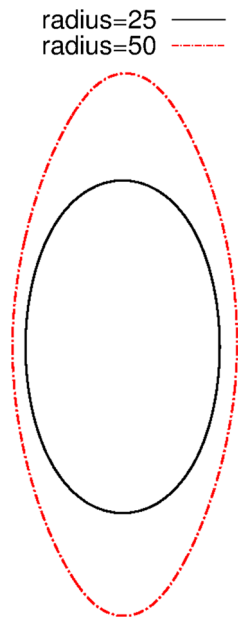


Fig. 8—Equilibrium shapes of precipitate with tetragonal misfit and different sizes $R = 25$ ($L = 2.08$) and $R = 50$ ($L = 4.16$), $A_z = 3.0$, $t = +2.0$, $\delta = 1.0$.

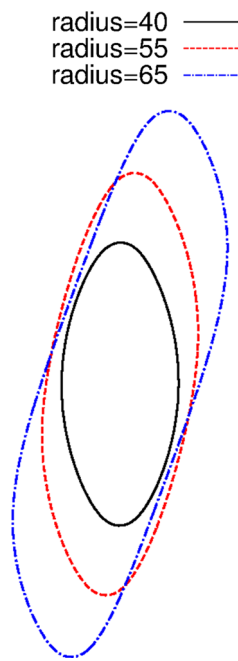


Fig. 9—Equilibrium shapes of precipitate with tetragonal misfit and with varying precipitate sizes, below bifurcation point, *i.e.*, $R = 40$ ($L = 3.3$) and above $R = 55$ ($L = 4.59$) and $R = 65$ ($L = 5.42$), $A_z = 0.3$, $t = +2.0$, $\delta = 1.0$.

ellipse-like morphology, which is elongated along the direction of least misfit. However, with increase in the size of precipitate, its morphology changes from an ellipse-like shape to a twisted diamond like shape as shown in the Figure 9. Here, the precipitates with equivalent radii of $R = 55$ and 65 have lost their mirror symmetry that is observed for the smaller sizes.

This shape bifurcation can be understood as a competition between the tendency of the precipitate to align along the elastically soft direction that is $\langle 110 \rangle$ corresponding to the choice of $A_z = 0.3$ and the tetragonality influencing the shape towards an elongated ellipse in the y -direction. The precipitate with smaller sizes tends to align along the lower misfit directions, while beyond the critical point the bifurcated shapes reflect the combined influence of both the elastic anisotropy and the tetragonality resulting in a twisted diamond shape with an orientation in between the lower misfit direction ($\langle 100 \rangle$) and elastically soft direction ($\langle 110 \rangle$).

Here, we will follow the same procedure as adopted in the previous sections. We compare the morphologies of the precipitate obtained from the phase-field simulations with FEM, which is illustrated in Figure 10 for a given condition where ($R = 75$), $A_z = 0.3$, $\delta = 1.0$, and $t = 2$. Again, we find an excellent agreement between the shapes computed from both numerical methods. In both the cases, the volume occupied by the precipitates is the same as well as both the precipitates are inclined similarly. Differences occur along the extended directions, where the curvatures from the FEM simulated shapes are slightly smaller compared to the ones produced from the phase-field simulations, which again

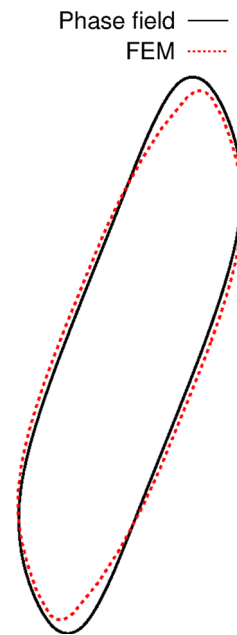


Fig. 10—The comparison between equilibrium shapes of precipitate with equal area, obtained from the phase-field and FEM results, $R = 75$ ($L = 6.25$), $A_z = 0.3$, $t = +2.0$, $\delta = 1.0$.

given the increased spatial resolution of the phase-field method is not surprising.

In order to derive the bifurcation diagram, we have calculated the shape factor (ρ) as a function of the precipitate size, *i.e.*, characteristic length (L). The shape factor in this situation can be defined as follows:

$$\rho = \sum_{i=1}^N \frac{X_i Y_i}{NV}, \quad [43]$$

where X_i , Y_i are the coordinates on the precipitate–matrix interface considering the center of mass of the precipitate is at the origin; N is the total number of interfacial points and V is the volume of precipitate. This definition of the shape factor ensures that it is equal to zero when the precipitate has mirror symmetry along the direction of least misfit, *i.e.*, the precipitate morphology is ellipse-like or elongated diamond, whereas it has non-zero values for a twisted diamond like shape.

Figure 11 depicts the calculated bifurcation diagram, which contains the results obtained from both the phase-field as well as FEM simulations. We get a continuous transition of the shape factor beyond the bifurcation point from the phase-field results, whereas the FEM results also give continuous transition but with a small jump at the bifurcation point and beyond. Phase-field results show that the shape bifurcation occurs at a characteristic length of 3.41, whereas FEM simulations predict 3.49. It is observed that beyond the bifurcation point the shape factors retrieved from the phase-field computations deviate from that of the FEM predictions. This difference in the calculations might be due to the increased complexity in the shape which is possibly better resolved by the phase-field method.

In order to ensure that the phase-field calculations are indeed yielding the lowest energy shapes, we have computed the equilibrium shapes beyond the bifurcation point which are ellipse-like (elongation along y -direction). This is done by starting with an initial configuration that is an ellipse with its long axis perfectly

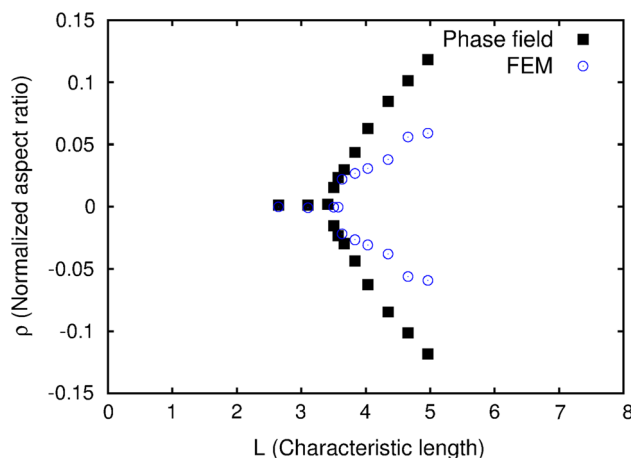


Fig. 11—Shape bifurcation diagram for misfit ratio $\iota = 2.0$, comparison between phase-field and FEM results ($A_z = 0.3$, $\delta = 1.0$), where ρ is plotted as a function of characteristic length.

aligned with the y -axis, at $x = 0$. Thereafter, we have calculated corresponding total energies of the precipitates as highlighted in Figure 12, as a function of characteristic length. It is observed that the total energy of the twisted diamond like shapes is lower than that of the precipitates which are ellipse-like. This indicates that the precipitates with lower energies (twisted diamond shape) are the stabler equilibrium configurations, compared to their ellipse-like counterparts, beyond the bifurcation point. Thus as shown in Figure 13, if we give a slight rotation to an ellipse-like precipitate (thick dark line), it will acquire a twisted diamond-like shape (dotted line) as an equilibrium state, beyond the critical point. With increase in the characteristic length past the bifurcation point, the difference between the total

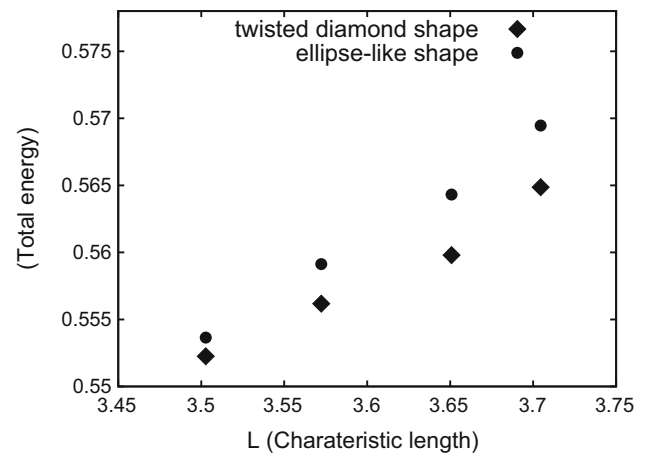


Fig. 12—Variation of the elastic energy of precipitate as a function of characteristic length (L) for ellipse-like precipitate (circle) and twisted diamond shape of precipitate (diamond).

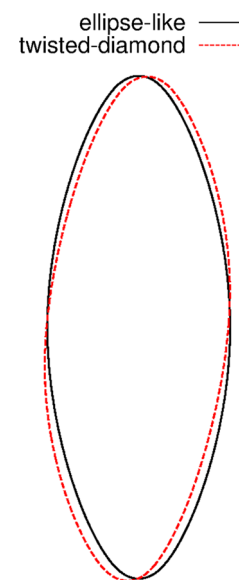


Fig. 13—The equilibrium shapes of precipitate with same equivalent radius $R = 52$ ($L = 3.5$), ellipse-like shape (thick dark line) in metastable equilibrium and diamond-like shape (dotted red-line) in stable equilibrium (Color figure online).

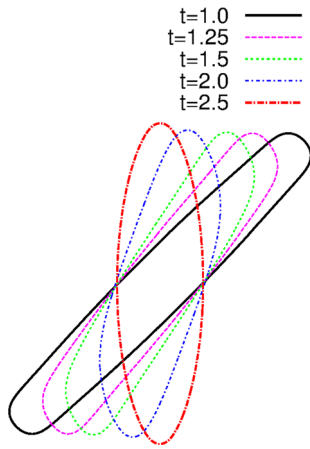


Fig. 14—Equilibrium morphologies of precipitate with varying degree of strength of tetragonal misfit which varies from $t = 1.0$ to 2.5 for $A_z = 0.3$, $\delta = 1.0$.

energies of stable and metastable precipitate shapes keeps on increasing.

As illustrated in the previous section, the change exhibited in the precipitate morphology is an effect of the precipitate size alone, where the misfit ratio remains constant, *i.e.*, $t = 2.0$. Further, we also characterize the effect of change in the magnitude of misfit ratio, *i.e.*, $\epsilon_{xx}^*/\epsilon_{yy}^*$ on the equilibrium morphologies of the precipitate by keeping the size constant. For this purpose, we keep the magnitude of ϵ_{xx}^* constant and varied ϵ_{yy}^* from 0.004 to 0.01. Accordingly, the misfit ratio takes values from 2.5 to 1.0. Figure 14 shows the equilibrium shapes of the precipitate for the different values of misfit ratio with $A_z = 0.3$, $\delta = 1.0$. Here, we retain the same precipitate size for all calculations (*i.e.*, $R = 65$). As discussed earlier, with these conditions the precipitate acquires a bifurcated shape which is twisted diamond like. With increase in the magnitude of misfit ratio, the precipitate orientation changes towards the direction of least misfit, *i.e.*, the vertical axis. Initially, for $t = 1.0$, the equilibrium precipitate is aligned exactly along the elastically softer directions which are $\langle 110 \rangle$ with an orientation of 45 deg alongside a rectangular shape, *i.e.*, in this case the equilibrium shape is determined by the elastically softer directions ($A_z = 0.3$) alone. As the misfit ratio elevates from 1.0 to higher values, the precipitate acquires an orientation with the larger magnitude, which is an obvious situation, as the orientation is a compromise between the tendencies to align along the elastically softer direction ($\langle 110 \rangle$) and the direction of lower misfit (010). For $t = 2.5$, an equilibrium morphology tends towards elongation along the lower misfit directions, where the precipitate has an elongated ellipse-like shape aligned along the vertical axis. This is again reflected in Figure 15, where the magnitude of the shape factor goes to zero as the magnitude of misfit ratio becomes larger. The other way of looking at this is that with increase in the magnitude of the misfit ratio the bifurcation point for the system shifts to larger values of equivalent precipitate sizes, as

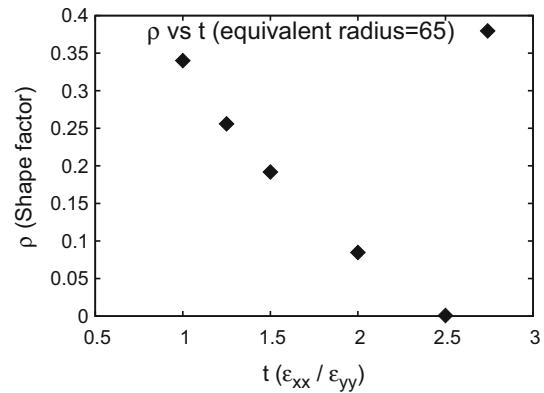


Fig. 15—Plot depicts the change in shape factor as function of misfit ratio varying from $t = 1.0$ to 2.5 for $A_z = 0.3$, $\delta = 1.0$.

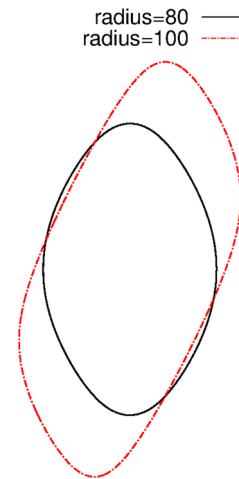


Fig. 16—Equilibrium shapes of precipitate with tetragonal misfit and different sizes, where $R = 80$ ($L = 6.66$) and $R = 100$ ($L = 8.33$), $A_z = 2.0$, $t = -2.0$, *i.e.*, $\epsilon_{xx}^* = 0.01$, $\epsilon_{yy}^* = -0.005$.

the driving force for the precipitate elongating along the direction of lower misfit increases.

2. Misfit components with opposite sign

In this case, the misfit components along x - and y -directions have opposite sign as well as different magnitude. Here, we have chosen $t = -2.0$, *i.e.*, $\epsilon_{xx}^* = 0.01$, $\epsilon_{yy}^* = -0.005$ and $A_z = 2.0$. Although, the symmetry of misfit is the same as compared with the previous section, there is an important difference. As shown in Figure 16, there is a shape transition in this case too, where a precipitate with size $R = 80$, has an ellipse-like shape, while above the critical characteristic length, precipitate ($R = 100$), a twisted diamond like shape results as the equilibrium morphology. This shape transition is seen in all the cases where $A_z < 1.0$, 1.0 and > 1.0 . So, the shape bifurcation occurs even at $A_z = 1.0$ and $A_z > 1.0$, which is in contrast to the previous case where the principal components of misfit strains have the same sign.

Figure 17, also shows that the precipitate with a smaller radius ($R = 40$) and A_z less than one ($A_z = 0.3$),

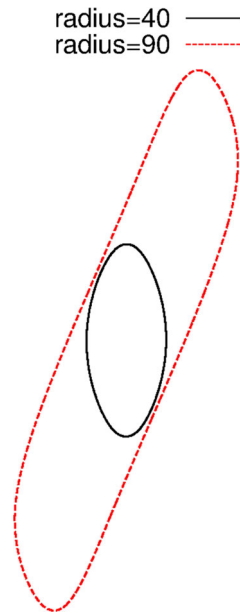


Fig. 17—Equilibrium shapes of precipitate with tetragonal misfit and different sizes, where $R = 40$ ($L = 3.33$) and $R = 90$ ($L = 7.5$), $A_z = 0.3$, $t = -2.0$, *i.e.*, $\epsilon_{xx}^* = 0.01$, $\epsilon_{yy}^* = -0.005$.

has an equilibrium shape which has its axis elongated along the direction of lower misfit. For the larger precipitate shapes ($R = 90$), we acquire a twisted diamond like shape. It is observed that there is an influence of the change in magnitude of inhomogeneity moduli (δ) and the magnitude of Zener anisotropy parameter (A_z) on the critical characteristic length (L_c) of shape bifurcation. For a systematic analysis, we keep δ constant ($\delta = 1.0$), *i.e.*, the homogeneous moduli, while the Zener anisotropy parameter (A_z) is varied from 0.3 to 2.0. We noticed that the L_c is lower for $A_z = 0.3$ compared to the case of $A_z = 2.0$. For $A_z = 0.3$, the precipitates with smaller sizes acquire a twisted diamond-like shape, as $\langle 110 \rangle$ are elastically softer directions. This provides a driving force for the precipitates even with the smaller sizes to orient along the elastically softer directions. In contrast for $A_z > 1.0$ (in this case $A_z = 2.0$), the elastically soft direction are $\langle 100 \rangle$ which is also the same as the direction of lowest misfit. Thus, it becomes harder for the precipitates to orient along $\langle 110 \rangle$ direction and acquire the twisted diamond like shape. This is evident from Figure 16, where we also find that the critical characteristic length (L_c) is pushed to larger values, *i.e.*, the shape transition occurs for the larger precipitate sizes.

E. Competition Between Anisotropy in Interfacial Energy and Elastic Energy

This section illustrates two factors controlling the selection of orientation of the precipitate morphology, *i.e.*, the anisotropies in interfacial energy (ϵ) and elastic energy (A_z). In order to investigate the influence of this competitive nature of the energy anisotropies, we first vary the anisotropy in elastic energy by changing the magnitude of A_z (with constant tetragonality, *i.e.*, $t =$

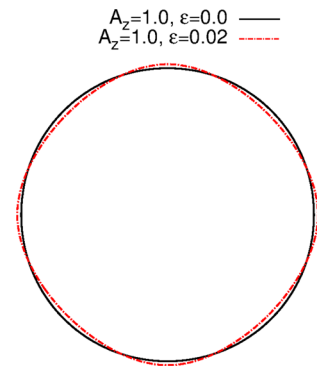


Fig. 18—Equilibrium shapes of precipitate with (red-dotted line) and without (thick dark line) anisotropy in interfacial energy, for $A_z = 1.0$, $t = 1$ (Color figure online).

$+1.0$), while keeping the anisotropy in interfacial energy constant and then repeat the other way around. This is achieved by incorporating anisotropy in interfacial energy as elaborated in Reference 49:

$$\begin{aligned} \gamma &= \gamma_0 a(\mathbf{n}), \\ \gamma &= \gamma_0 \left(1 - \epsilon \left(3 - 4 \frac{\phi_x'^4 + \phi_y'^4}{(\phi_x'^2 + \phi_y'^2)^2} \right) \right), \end{aligned} \quad [44]$$

where ϵ is the strength of anisotropy in interfacial energy; $a(\mathbf{n})$ is the anisotropy function of the interface normal \mathbf{n} , which has components $\mathbf{n}_x = -\frac{\phi_x'}{|\nabla\phi|}$, $\mathbf{n}_y = -\frac{\phi_y'}{|\nabla\phi|}$, with ϕ_x' and ϕ_y' being the partial derivatives of the order parameter $\phi(x, y)$ in the x and y -directions.

1. Effect of anisotropy in elastic energy (A_z)

Here, the magnitude of A_z is altered from 0.3 to 3.0 for a constant $\epsilon = 0.02$. Figures 18 through 20 show the equilibrium precipitate morphologies with (dotted line) and without (thick line) anisotropy in interfacial energy, with increasing strength of A_z . In all the cases, the size of precipitate is kept the same, *i.e.*, the equivalent radius is constant ($R = 25$). In this regard, three prominent cases are investigated, *i.e.*, $A_z = 0.3$, 1.0 and 3.0, where the influence of the change in magnitude of A_z on the equilibrium morphology is discussed. All these simulations are performed with the precipitate sizes which are well below the bifurcation point.

In the first case, we keep $A_z = 1.0$, with $\epsilon = 0.02$. This is to quantify the effect of anisotropy in interfacial energy alone. The results are summarized in Figure 18, where the precipitate takes a circular shape (thick dark line) due to isotropic elastic energy with no anisotropy in interfacial energy. With the introduction of anisotropy in interfacial energy, the precipitate turns to a diamond like shape, with its faces parallel to $\langle 110 \rangle$ directions. So, the equilibrium shape of the precipitate is primarily determined by interfacial anisotropy alone.

Figure 19 shows an equilibrium precipitate morphology (thick dark line) with $A_z = 3.0$, where there is a cubic anisotropy in the elastic energy which drives the precipitate to acquire a square-like shape with rounded corners where the square faces are aligned along the

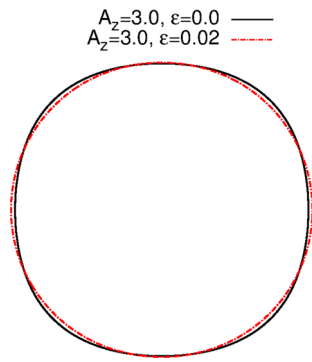


Fig. 19—Equilibrium shapes of precipitate with (red-dotted line) and without (thick dark line) anisotropy in interfacial energy, for $A_z = 3.0$, $t = 1$ (Color figure online).

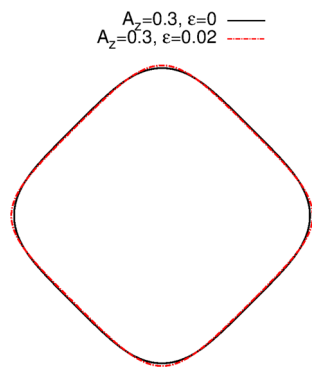


Fig. 20—Equilibrium shapes of precipitate with (red-dotted line) and without (thick dark line) anisotropy in interfacial energy, for $A_z = 0.3$, $t = 1$ (Color figure online).

elastically soft directions $\langle 100 \rangle$. Again, incorporating anisotropy in interfacial energy ($\varepsilon = 0.02$) tends to align the precipitate faces along $\langle 110 \rangle$ directions. This minimizes the effect of elastic anisotropy on precipitate shape, by giving rise to a morphology which takes a shape in between a square and a diamond. This is shown in Figure 19, where the equilibrium shape of the precipitate (dotted line) has acquired a shape as explained above. There can be a possibility, where effect of both anisotropies counterbalance each other and gives rise to a morphology that is circular, though the respective energies (elastic and interfacial) possess anisotropies.

When $A_z < 1$ (in this case $A_z = 0.3$), the precipitate acquires a shape which prefers to align its face along $\langle 110 \rangle$ directions that is elastically softer. This is captured in Figure 20, which shows the precipitate morphologies where both the interfacial and elastic anisotropies drive the precipitate shape towards a diamond. Precipitate without anisotropy in interfacial energy has its faces parallel to $\langle 110 \rangle$ directions, whereas with anisotropy in interfacial energy the precipitate faces become weakly concave towards the center of the precipitate with the corners becoming sharper. It is evident that the presence of interfacial anisotropy along with cubic anisotropy in elastic energy affects equilibrium morphologies of the precipitate distinctly.

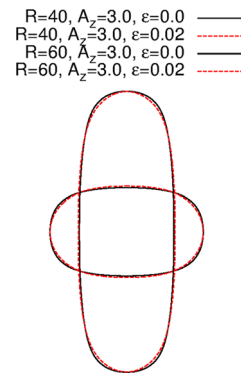


Fig. 21—Equilibrium shapes of precipitate beyond bifurcation point with (red-dotted line) and without (thick dark line) anisotropy in interfacial energy, for $A_z = 3.0$, $t = 1$ (Color figure online).

In the preceding discussion, we characterize the effect of energy anisotropies on the precipitate shape where the precipitate size is well below the bifurcation point (L_c). Now, we shift beyond the bifurcation point (L_c) with the same argument, *i.e.*, competitive effect of both the anisotropies while accessing the larger precipitate sizes. Figure 21 shows such morphologies of the precipitate with $A_z = 3.0$. Precipitates with two different sizes ($R = 40$ and 60) and different variants are shown. The presence of anisotropy in interfacial energy does not affect the equilibrium morphology of precipitate significantly, whereby though the precipitate corners become more rounded, edges of the precipitate remain strongly aligned along the elastically softer directions ($\langle 100 \rangle$). This implies that with increase in the size of precipitate, the influence of elastic energy anisotropy dominates over interfacial energy anisotropy.

2. Effect of anisotropy in interfacial energy (ε)

While in the previous section, the strength of anisotropy in interfacial energy (ε) is kept constant, furthering the discussion, in this section, we will consider the effect of varying ε on the precipitate morphology. Here, we vary the magnitude of ε from 0.0 to 0.04, while holding the Zener anisotropy parameter constant, at a value of $A_z = 3.0$. The equilibrium morphology of the precipitate initially acquires a cubic shape with rounded corners, while the precipitate faces are aligned along the elastically soft directions ($\langle 100 \rangle$). Further, with increase in the strength of ε , the precipitate faces start to orient towards $\langle 110 \rangle$ directions. This is due to a significant increase in the strength of anisotropy in interfacial energy, while keeping the magnitude of A_z constant. Thus, an increase in the strength of anisotropy in interfacial energy imparts a driving force for alignment of the precipitate faces along $\langle 110 \rangle$ directions rather than $\langle 100 \rangle$ directions (elastically softer), giving rise to a diamond-like shape as shown in Figure 22.

The characterization of change in the precipitate morphology is precisely captured by plotting the shape factor (η) as a function of the strength of elastic anisotropy for a given strength of anisotropy in interfacial energy, which is shown in Figure 23. Here, the

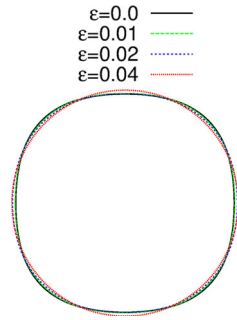


Fig. 22—The variation of equilibrium shapes of precipitate as a function of strength of interfacial anisotropy where ε varies from 0 to 0.04 and $A_z = 3.0$, $t = 1$.

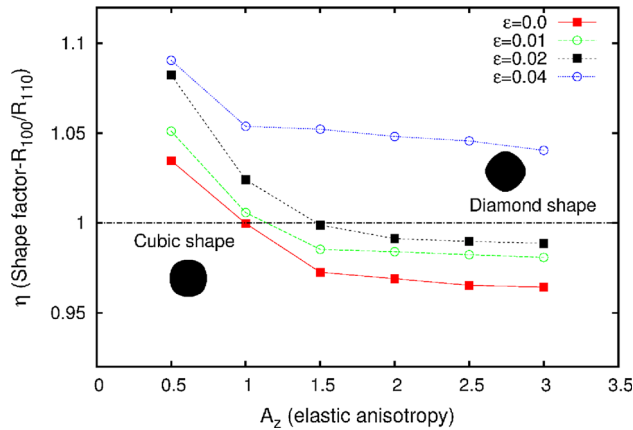


Fig. 23—Map represents the shape factor (η) as function of A_z for different strengths of interfacial anisotropy; dark horizontal line separates the region between cube (square)-like shapes of precipitate and diamond-like shapes of precipitates which are characterized by η .

shape factor is defined as the ratio of the precipitate size along $\langle 100 \rangle$ to size along $\langle 110 \rangle$. The significance of calculating η in this way is that it determines the precipitate orientation. If $\eta < 1.0$, it implies that the precipitate faces are aligned along the elastically soft directions, *i.e.*, $\langle 100 \rangle$ directions and the anisotropy in elastic energy is the shape determining factor provided $A_z > 1.0$. Similarly, if $\eta > 1.0$, it implies that the precipitate faces preferentially align along $\langle 110 \rangle$ directions which is determined by the anisotropy in interfacial energy and $\eta = 1.0$ gives a circular shape of the precipitate. Figure 23 depicts a morphology map, which plots the shape factor as a function of the different anisotropy strengths in the elastic energy A_z , while considering different values of anisotropy in interfacial energy ε . While for the case where $\varepsilon \leq 0.02$, there is a critical value beyond which the shape transition occurs from a diamond to a cube, for the larger values of anisotropy in interfacial energy, the equilibrium shape remains diamond like. The morphology map depicts that the morphology of the precipitate corresponding to $A_z = 1.5$ and $\varepsilon = 0.02$ acquires a near circular shape. However, this transition point is a function of the size of the precipitate.

F. Comparison with Experimental Results

In this paper, our focus is theoretical in extent; however, in this section we make possible connections with microstructures in experiments that may be referred to as equilibrium shapes of precipitates. It is noteworthy that such comparisons are non-trivial as the experimental conditions giving rise to a particular shape of the precipitate may not be equivalent to the boundary conditions in the simulations. For example, even at very low volume fractions of the second phase, with increase in the precipitate size, the elastic fields around the precipitates may interact with each other that may influence the precipitate size at which symmetry breaking shape transitions are observed. On the contrary, in the simulation, the precipitate is isolated in the sense that there is no interaction of elastic fields of the neighboring precipitate. With this disclaimer, we point to certain experimental reports of microstructures that bear similarity to our work.

Fahrman *et al.*^[50] have studied the series of low volume fraction Ni-Al-Mo alloys, with varying Mo-content. In this paper, the authors report a change in the shapes of the precipitate from a spherical to cubic morphology and a break in symmetry for larger precipitate sizes where cuboidal shapes are observed. The sizes at which the shape transition occurs are reported to be a function of the Mo-content which in turn is thought to influence the effective misfit at the interface. This finding of the authors is qualitatively in agreement with the equilibrium shape transitions obtained in our phase-field simulations with changes in the values of the dilatational misfit and strength of cubic anisotropy in elastic energy (see Section III-C).

An aspect of our paper is to construct a general framework using which equilibrium shapes of the precipitate with tetragonal misfit at the interface have been computed as a function of different variables such as misfit ratio (t), precipitate size (R), and sign of misfit at the interface (refer Section III-D). We have seen that below the bifurcation point, the shape of the precipitate is elongated diamond like, while with increase in the precipitate size the morphology turns towards a twisted diamond-like shape which is also referred to as S-shape precipitates by Voorhees *et al.*^[11] In their study, they mention that these S-shapes of precipitates are qualitatively consistent with shape of precipitates observed experimentally in Mg-stabilized ZrO₂.^[51] Lanteri *et al.*^[52] have stated that the ZrO₂ precipitates acquire tetragonal morphologies and associate it with the accommodation of the coherent strains at the interface due to a lattice misfit between the precipitate (t-ZrO₂) and the matrix (c-ZrO₂).

IV. COMPARISON WITH PREVIOUS MODELS

In this section, we compare our diffuse-interface model against the previous/available models for the calculation of equilibrium morphologies of precipitates. Here, as a starting point, it is useful to analyze the sharp-interface limit of the model as this will enable

comparison with other models which are either based on the level-set algorithm, FEM, boundary-integral methods or diffuse-interface methods.

For this, we recall the evolution equation, as in Eq. [4], written for simplicity for the case of isotropic interfacial energy. We transform this equation into a coordinate system that is normal to the interface at a given location where the order parameter is being updated. Thus, the interface normal $\nabla\phi$ can be written as

$$\nabla\phi = \mathbf{n} \frac{\partial\phi}{\partial n}, \quad [45]$$

which upon taking a divergence yields

$$\nabla^2\phi = \frac{\partial^2\phi}{\partial n^2} + \frac{\partial\phi}{\partial n}(\nabla \cdot \mathbf{n}). \quad [46]$$

Therefore, the transformed equation reads

$$\begin{aligned} \tau W \frac{\partial\phi}{\partial t} = 2\gamma W \left(\frac{\partial^2\phi}{\partial n^2} + \frac{\partial\phi}{\partial n}(\nabla \cdot \mathbf{n}) \right) - \frac{16}{\pi^2} \frac{\gamma}{W} (1 - 2\phi) \\ - \frac{\partial f_{\text{el}}}{\partial\phi} - \lambda_\beta h'(\phi). \end{aligned} \quad [47]$$

The leading order solution for the phase-field profile ϕ^0 satisfies the equation:

$$2\gamma W \frac{\partial^2\phi^0}{\partial n^2} - \frac{16}{\pi^2} \frac{\gamma}{W} (1 - 2\phi^0) = 0, \quad [48]$$

which upon integration once along the interface normal along with the boundary conditions that in the bulk precipitate and the matrix $\frac{\partial\phi^0}{\partial n} = 0$, gives

$$\gamma W \left(\frac{\partial\phi^0}{\partial n} \right)^2 = \frac{16}{\pi^2} \frac{\gamma}{W} \phi^0 (1 - \phi^0), \quad [49]$$

the solution to this is also the equilibrium phase-field profile without any driving forces. Along with this, the leading order solutions to the stress-strain profiles are determined from mechanical equilibrium conditions, in the limit that the interface thickness tends to zero. Without extensive math and drawing from the results of the phase-field simulations which deliver the stress-strain profiles along the interface normal (see A.2 in the Appendix), we see that in the limit of vanishing interface thickness, where the values of the properties at the interface and the asymptotic extensions from the bulk on either side onto the interface become the same for the continuous variables and constitute a jump at the interface for the discontinuous variables. Thereby the following conditions will be satisfied:

$$\begin{aligned} \sigma_{\text{nn}}^\alpha = \sigma_{\text{nn}}^\beta = \sigma_{\text{nn}}^0, \\ \sigma_{\text{nt}}^\alpha = \sigma_{\text{nt}}^\beta = \sigma_{\text{nt}}^0, \end{aligned} \quad [50]$$

which is also consistent with the condition for zero traction along the normal, while the strains,

$$\epsilon_{\text{tt}}^\alpha = \epsilon_{\text{tt}}^\beta = \epsilon_{\text{tt}}^0, \quad [51]$$

are continuous across the interface. The other components, however, are going to exhibit a jump across the interface. These are same jump conditions we utilize in the tensorial interpolation scheme and also elaborated in Reference 46. Using the preceding arguments, the leading order phase-field update derives as

$$\tau W \frac{\partial\phi}{\partial t} = 2\gamma W \frac{\partial\phi^0}{\partial n} (\nabla \cdot \mathbf{n}) - \frac{\partial f_{\text{el}}}{\partial\phi} - \lambda_\beta h'(\phi). \quad [52]$$

Additionally, using the sharp-interface limits of the stress and strain profiles, we can also derive the following:

$$\begin{aligned} \frac{\partial f_{\text{el}}}{\partial\phi} = \frac{df_{\text{el}}}{d\phi} - \frac{\partial f_{\text{el}}}{\partial\epsilon_{\text{nn}}} \frac{\partial\epsilon_{\text{nn}}}{\partial\phi} - 2 \frac{\partial f_{\text{el}}}{\partial\epsilon_{\text{nt}}} \frac{\partial\epsilon_{\text{nt}}}{\partial\phi} \\ - \frac{\partial f_{\text{el}}}{\partial\epsilon_{\text{tt}}} \frac{\partial\epsilon_{\text{tt}}}{\partial\phi}. \end{aligned} \quad [53]$$

Since, in the sharp-interface limit, the strain component ϵ_{tt} is continuous across the interface the last differential in the preceding equation vanishes, in the limit that the interface thickness becomes zero, thereby the leading order elastic driving force derives as

$$\begin{aligned} \frac{\partial f_{\text{el}}}{\partial\phi} = \frac{df_{\text{el}}}{d\phi} - \sigma_{\text{nn}}^0 \frac{\partial\epsilon_{\text{nn}}}{\partial\phi} - 2\sigma_{\text{nt}}^0 \frac{\partial\epsilon_{\text{nt}}}{\partial\phi} \\ = \frac{d}{d\phi} (f_{\text{el}} - \sigma_{\text{nn}}^0 \epsilon_{\text{nn}} - 2\sigma_{\text{nt}}^0 \epsilon_{\text{nt}}). \end{aligned} \quad [54]$$

Substituting in the leading order phase-field update as in Eq. [52], we derive

$$\begin{aligned} \tau W \frac{\partial\phi}{\partial t} = 2\gamma W \frac{\partial\phi^0}{\partial n} (\nabla \cdot \mathbf{n}) - \frac{d}{d\phi} (f_{\text{el}} - \sigma_{\text{nn}}^0 \epsilon_{\text{nn}} - 2\sigma_{\text{nt}}^0 \epsilon_{\text{nt}}) \\ - \lambda_\beta h'(\phi). \end{aligned} \quad [55]$$

Multiplying both sides of the preceding equation with the normal derivative of the leading order phase-field profile, $\frac{\partial\phi^0}{\partial n}$, and integrating from inside the bulk precipitate into the matrix in the normal direction, we derive

$$\begin{aligned} \int_{\text{in}}^{\text{out}} \tau W \frac{\partial\phi}{\partial t} \frac{\partial\phi^0}{\partial n} dn = 2\gamma W \int_{\text{in}}^{\text{out}} \left(\frac{\partial\phi^0}{\partial n} \right)^2 (\nabla \cdot \mathbf{n}) dn \\ - \int_1^0 \frac{d}{d\phi} (f_{\text{el}} - \sigma_{\text{nn}}^0 \epsilon_{\text{nn}} - 2\sigma_{\text{nt}}^0 \epsilon_{\text{nt}}) d\phi \\ - \int_1^0 \lambda_\beta h'(\phi) d\phi. \end{aligned} \quad [56]$$

Using the property that, $\frac{\partial \phi}{\partial t} \frac{\partial \phi^0}{\partial n} = -\left(\frac{\partial n}{\partial t}\right)_\phi \left(\frac{\partial \phi^0}{\partial n}\right)^2 = -v_n \left(\frac{\partial \phi^0}{\partial n}\right)^2$, where additionally $\left(\frac{\partial n}{\partial t}\right)_\phi$ is replaced with the normal velocity v_n . Further, $\nabla \cdot \mathbf{n} = -\kappa$ (ignoring changes of curvature along the interface normal) thereby the following equation is derived:

$$\begin{aligned} -\tau W v_n \int_{\text{in}}^{\text{out}} \left(\frac{\partial \phi^0}{\partial n}\right)^2 dn &= -2\gamma W \kappa \int_{\text{in}}^{\text{out}} \left(\frac{\partial \phi^0}{\partial n}\right)^2 dn \\ &\quad - (f_{\text{el}} - \sigma_{\text{nn}}^0 \epsilon_{\text{nn}} - 2\sigma_{\text{nt}}^0 \epsilon_{\text{nt}})|_1^0 \\ &\quad - \lambda_\beta h(\phi^0)|_1^0. \end{aligned} \quad [57]$$

Using the relation, in Eq. [49], we can integrate $\int_{\text{in}}^{\text{out}} \left(\frac{\partial \phi^0}{\partial n}\right)^2 dn$ as $\int_1^0 \left(\frac{\partial \phi^0}{\partial n}\right) d\phi$, or, $-\int_1^0 \frac{4}{\pi W} \sqrt{\phi^0(1-\phi^0)} d\phi^0$, that returns $\frac{1}{2W}$. Combining the results into the preceding equation, we derive

$$\frac{1}{2} \tau v_n = \gamma \kappa + (\omega_\beta - \omega_\alpha) - \lambda_\beta, \quad [58]$$

where we have assigned $\omega = (f_{\text{el}} - \sigma_{\text{nn}}^0 \epsilon_{\text{nn}} - 2\sigma_{\text{nt}}^0 \epsilon_{\text{nt}})$. The preceding sharp-interface limit is a relation between the velocity of advance of the interface front as result of the capillarity forces $\gamma \kappa$ as well as the elastic configurational forces $(\omega_\beta - \omega_\alpha)$, while the Lagrange parameter λ_β maintains the volume constraint. This is similar to the condition that is derived by Zhao *et al.*,^[23,24] wherein $(\omega_\beta - \omega_\alpha)$ is nothing but the term $\mathbf{n} \cdot (\Sigma_\beta - \Sigma_\alpha) \cdot \mathbf{n}$, with Σ being the Eshelby momentum tensor $(f_{\text{el}} I - \sigma \cdot \nabla \mathbf{u})$ ^[53] (\mathbf{u} is the displacement field) that is used in the paper. Similarly, for the condition of equilibrium, v_n is identically zero at all the interface points for which we have

$$\lambda_\beta = \gamma \kappa + (\omega_\beta - \omega_\alpha). \quad [59]$$

Comparing this with the balance condition that is utilized in the work by Thomson and Voorhees,^[10] to generate the set of integro-differential equations for the solutions of the interface coordinates, λ_β is nothing but the difference of the chemical potential between the phases α and β for an uniform diffusion potential. This is also remarked in Schmidt and Gross,^[14] although the algorithms of arriving at the interface solutions are different. Also, for the more generic case in the presence of interfacial energy anisotropy, $\gamma \kappa$ should be replaced with $\nabla \cdot \xi$, where ξ is the Cahn–Hoffmann zeta vector^[54] as in Reference 10, and which can be also shown in the present phase-field model in the sharp-interface limit. The advantage in our phase-field model is that with just a slightly additional cost of resolving the diffuse-interface model, complicated shapes may be simulated in all dimensions with quite simple discretization techniques than the ones employed in the FEM as well as level-set methods. A more subtle point but noteworthy is that the term $(\omega_\beta - \omega_\alpha)$ is exactly the same that results from $\frac{\partial f_{\text{el}}}{\partial \phi}$ in the tensorial interpolation scheme that we describe in

the section on the model formulation. The tensorial interpolation exactly utilizes the jump conditions of the stress and the strain profiles in the sharp-interface limit in the interpolation of the elastic energies of the individual phases.

Our present formulation of the phase-field model is in contrast to other contemporary models such as in References 27, 28, 35, and 55, that use the modified Cahn–Hilliard equation, incorporating for elasticity. In these models, the misfit strains are enslaved as functions of the composition field, along with the values of the stiffness tensor across the interface. The equilibrium morphology is derived by solving the modified Cahn–Hilliard evolution equation until the diffusion potential is the same everywhere. In terms of computational efficiency, this is more costly than our model because our evolution equation concerns the update of the order parameter ϕ whose variation is only over a finite length defined by the diffuse-interface region that is much smaller in extent compared to the corresponding solution of the composition field over the entire integration domain. Apart from this, there is also a physical difference which stems from the fact that our misfits and stiffness tensors are enslaved to the value of the order parameter ϕ . This implies that the condition of diffusional and mechanical equilibrium may be decoupled as is the situation in the classical Johnson and Cahn model^[9] or the numerical FEM models,^[10,14,17,23,27] where the composition in the matrix and precipitate satisfies just the Laplace equation with the constraint of the same diffusion potential. However, for the diffuse-interface models that use the composition to parameterize the variation of the misfits and stiffness across the interface, the diffusional and mechanical equilibrium problems become coupled. This entails that just the diffusion potential μ arising from the chemical part of the free energy is not constant in the domain, whereas it is the effective chemical potential $\mu - W \nabla^2 c - \sigma : \delta \epsilon^* h'(c) + \frac{1}{2} \delta \sigma : (\epsilon - \epsilon^*(c)) g'(c)$ that is same everywhere, where $\delta \epsilon^*$ is the difference of the eigenstrain between the phases, while $h(c)$ and $g(c)$ are interpolation functions of the scaled compositions, which smoothly go to fixed values in the bulk phases. $\delta \sigma = (C^\alpha - C^\beta)(\epsilon - \epsilon^*(c))$, where $\epsilon^*(c)$ is the interpolated eigenstrain. The interpolation functions $h(c)$ and $g(c)$ are typically chosen such that in the bulk their derivatives return zero that essentially implies that the modification to the boundary condition of the diffusion potential w.r.t. the sharp-interface problem is only at the interface. In the classical Cahn–Hilliard problem without elasticity, this variation of the diffusion-potential leads to a grand-potential excess at the interface, which when integrated across the interface determines the interfacial energy γ in the system. In the presence of elastic energies, the variation of the diffusion potential in the interface is modified and thereby also the interfacial energy. The interfacial energy therefore scales with the interface width W while being a function of the stress and strain distribution in the interface. Additionally, the interfacial compositions as well as the effective misfits and stiffness will exhibit a change along the interface between the precipitate and

the matrix, as the stresses vary with the direction of the normal to the interface. As argued by Leo *et al.*,^[27] such modifications scale with the value of the interface width W and in the limit of vanishing interface thickness the sharp-interface problem is retrieved. It is also important to mention that in our model formulation as well, the Khachaturyan-type interpolation does yield an interfacial excess which modifies the interfacial energy from the model parameter γ and the deviation scales with W , although the nature of the excess is different. This interfacial excess is removed with the tensorial interpolation as described in this paper and in Reference 46 as it respects the precise jump conditions corresponding to the sharp-interface problem. However, given the subtle but important conceptual difference between our model formulation and the other diffuse-interface models, it is presently unclear to us, which amongst the modeling schemes, will yield acceptable errors with respect to the sharp-interface problem, with the larger interface width W .

With regard to the actual situation experimentally, the misfit may truly be a strong function of the composition. The problem is even quite complicated in multi-component alloys, where given the different possible equilibria, the interesting situation is that the choice of the equilibrium compositions controls the magnitude of the misfit and thereby also the shape. The three factors are coupled and thereby it is unlikely that the misfit parameterization can be done as a function of the order parameter as performed in our model presentation or held as a constant value as in the classical analytical and FEM models. Consequently, the mechanical equilibrium and the equilibration of the composition field may need to be performed in a coupled fashion along with the solution to the Allen–Cahn equation for the order parameter update under the constraint of constant volume. This is similar to the chemo-mechanical model level-set-based FEM approach proposed by Zhao *et al.*,^[24] which also incorporates interfacial stresses. Extension of our model along these lines particularly for addressing the situations of multi-component alloys is possible.

V. CONCLUSION

In this paper, we have presented a phase-field model for the determination of equilibrium morphology of precipitates under coherency stresses. Our model couples the Allen–Cahn dynamics of the order parameter evolution with the constraints of mechanical equilibrium as well as volume constraint. Using this model, we predict the symmetry breaking transitions and bifurcation diagrams which occur for the shapes of the precipitates as a function of size, for various combinations of misfits as well as anisotropies in the elastic constants. These predictions are compared against available analytical solutions^[9] as well as sharp-interface computations^[17] where we find excellent agreement. In

the system with non-dilatational misfits, when misfits along principal directions have same sign, the shape transition (ellipse to twisted diamond shape) is observed only when $A_z < 1$, otherwise the precipitate keeps elongating along the axis of direction with lower misfit. When misfits along principal directions have opposite signs, the precipitate shape transition occurs irrespective of the magnitude of A_z . These results are in very good agreement with previous numerical results.^[17,18] Along with this we also study the combined influence of elastic and interfacial energy anisotropy both above and below bifurcation. Here, we find that in the presence of interfacial energy anisotropy, there is a continuous change in the shape of the precipitate with size before bifurcation, which is different from the case where there is just elastic anisotropy. We find that the modifications in the shape both above and below the bifurcation point do not change remarkably, although for certain combinations of strengths of the anisotropies in the interfacial and elastic energies a completely isotropic shape may be retrieved below the bifurcation point. It remains as a scope for future work to investigate the use of larger anisotropy strengths in the interfacial energy that could lead to facets in the equilibrium shapes. This will require regularization of the interfacial energy forms that have been performed in previous contributions from Eggleston *et al.*^[56] and Voigt and colleagues.^[57] Apart from this, we also compare and contrast our model formulation with other diffuse-interface and sharp-interface models. Here, while we discuss that the sharp-interface model descriptions are retrieved in the different diffuse-interface models in the sharp-interface limit, we also highlight the conceptual differences between our model formulation and the other diffuse-interface methods. Amongst the future outlooks, is the coupling of the Allen–Cahn dynamical equation with a time-dependent diffusional equation for the study of growth and coarsening of precipitates in multi-component systems.

ACKNOWLEDGMENTS

We thank Professor T. A. Abinandanan for many valuable inputs and insightful, stimulating discussions on the subject. We express our appreciation to Boeing-India for the support under the Project PC36032.

APPENDIX A

A.1 Elastic Free Energy Density

Equation [8] gives the elastic free energy density, which includes several pre-factors, *i.e.*, Z_3, Z_2, Z_1, Z_0 . These pre-factors are dependent on particular values of elastic constant in respective phases, *i.e.*, the precipitate and matrix. Their expressions are as follows: here $C_{11}^{\alpha,\beta} = C_{1111}^{\alpha,\beta}$, $C_{22}^{\alpha,\beta} = C_{2222}^{\alpha,\beta}$, $C_{44}^{\alpha,\beta} = C_{1212}^{\alpha,\beta}$, $C_{12}^{\alpha,\beta} = C_{1122}^{\alpha,\beta}$.

$$\begin{aligned}
Z_3 &= (C_{11}^\alpha - C_{11}^\beta + C_{12}^\alpha - C_{12}^\beta) \epsilon^{*2}, \\
Z_2 &= (C_{11}^\beta - C_{11}^\alpha) (\epsilon_{xx} + \epsilon_{yy}) \epsilon^* \\
&\quad + (C_{12}^\beta - C_{12}^\alpha) (\epsilon_{xx} + \epsilon_{yy}) \epsilon^* \\
&\quad + (C_{11}^\beta + C_{12}^\beta) \epsilon^{*2}, \\
Z_1 &= \frac{1}{2} (C_{11}^\alpha - C_{11}^\beta) (\epsilon_{xx} + \epsilon_{yy}) \epsilon^* \\
&\quad - C_{11}^\beta (\epsilon_{xx} + \epsilon_{yy}) \epsilon^* \\
&\quad + (C_{12}^\alpha - C_{12}^\beta) \epsilon_{xx} \epsilon_{yy} - \frac{1}{2} C_{12}^\beta (\epsilon_{xx} + \epsilon_{yy}) \epsilon_{yy} \\
&\quad + 2 (C_{44}^\alpha - C_{44}^\beta) \epsilon_{xy}^2, \\
Z_0 &= \frac{1}{2} (C_{11}^\beta (\epsilon_{xx}^2 + \epsilon_{yy}^2) + C_{44}^\beta \epsilon_{xy} + C_{12}^\beta \epsilon_{xx} \epsilon_{yy}).
\end{aligned}$$

A.2 Stress-Strain Profiles

See Figures 24, 25, 26 and 27

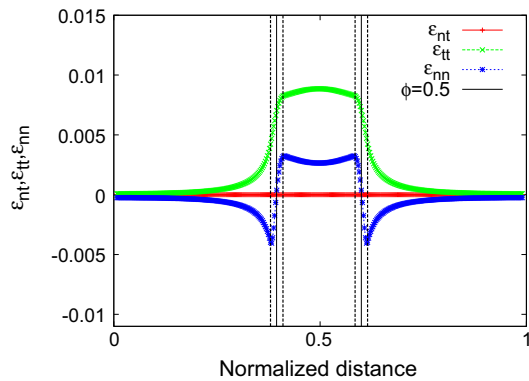


Fig. 24—1D section of strain profile obtained from 2D domain across the center of precipitate where the region occupied between the dotted lines represents the diffuse interface, at $\delta = 0.5$, $\mu_{\text{mat}} = 125$.

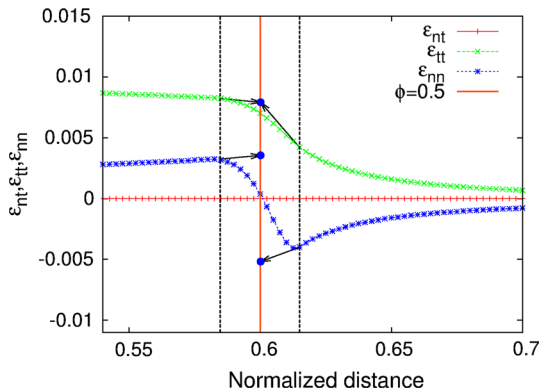


Fig. 25—The zoomed section of the interface showing strain profile across the center of precipitate, thick orange line passes through the interface at $\phi = 0.5$ (Color figure online).

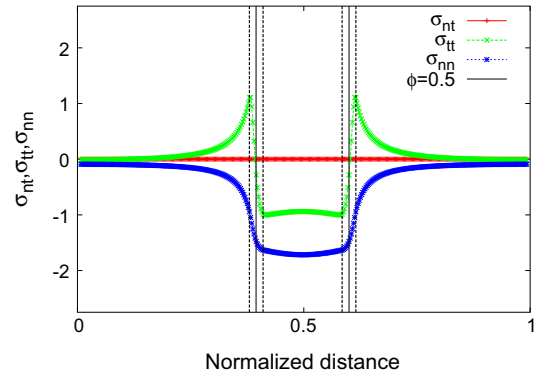


Fig. 26—1D section of stress profile obtained from 2D domain across the center of precipitate where the region occupied between the dotted lines represents the diffuse interface, at $\delta = 0.5$, $\mu_{\text{mat}} = 125$.

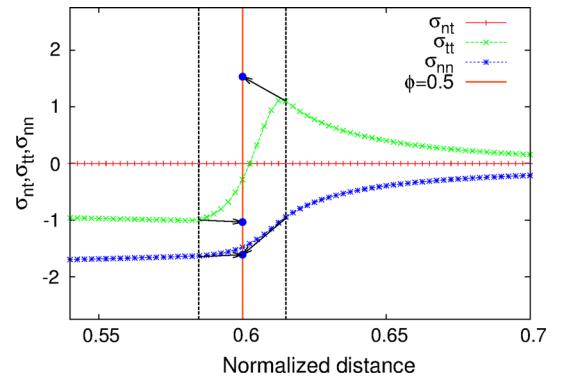


Fig. 27—The zoomed section of the interface showing 1D stress profile across the center of precipitate, thick orange line passes through the interface at $\phi = 0.5$ (Color figure online).

REFERENCES

1. J.G. Conley, M.E. Fine, and J.R. Weertman: *Acta Metall.*, 1989, vol. 37, pp. 1251–63.
2. A. Maheshwari and A.J. Ardell: *Scripta Metall. Mater. (US)*, 1992, vol. 26.
3. A.J. Ardell: *Metall. Mater. Trans. B*, 1970, vol. 1B, pp. 525–34.
4. P. Rastogi and A.J. Ardell: *Acta Metall.*, 1971, vol. 19, pp. 321–30.
5. D. Chellman and A. Ardell: *Acta Metall.*, 1974, vol. 22, pp. 577–88.
6. A. Ardell: *Metall. Trans. A*, 1985, vol. 16, pp. 2131–65.
7. D.N. Seidman, E.A. Marquis, and D.C. Dunand: *Acta Mater.*, 2002, vol. 50, pp. 4021–35.
8. T.M. Pollock and S. Tin: *J. Propuls. Power*, 2006, vol. 22, pp. 361–74.
9. W. Johnson and J. Cahn: *Acta metall.*, 1984, vol. 32, pp. 1925–33.
10. P.W. Voorhees, G. McFadden, and W. Johnson: *Acta Metall. Mater.*, 1992, vol. 40, pp. 2979–92.
11. M. Thompson, C. Su, and P. Voorhees: *Acta metall. mater.*, 1994, vol. 42, pp. 2107–22.
12. M. Thompson and P. Voorhees: *Acta mater.*, 1999, vol. 47, pp. 983–96.
13. X. Li, K. Thornton, Q. Nie, P. Voorhees, and J.S. Lowengrub: *Acta mater.*, 2004, vol. 52, pp. 5829–43.
14. I. Schmidt and D. Gross: *J. Mech. Phys. Solids*, 1997, vol. 45, pp. 1521–49.
15. I. Schmidt, R. Mueller, and D. Gross: *Mech. Mater.*, 1998, vol. 30, pp. 181–96.
16. R. Mueller and D. Gross: *Comput. Mater. Sci.*, 1998, vol. 11, pp. 35–44.

17. C. Jog, R. Sankarasubramanian, and T. Abinandanan: *J. Mech. Phys. Solids*, 2000, vol. 48, pp. 2363–89.
18. R. Sankarasubramanian, C.S. Jog, and T.A. Abinandanan: *Metal. Mater. Trans. A*, 2002, vol. 33A, pp. 1083–90.
19. H.J. Jou, P.H. Leo, and J.S. Lowengrub: *J. Comput. Phys.*, 1997, vol. 131, pp. 109–48.
20. S. Kolling, R. Mueller, and D. Gross: *Int. J. Solids Struct.*, 2003, vol. 40, pp. 4399–4416.
21. N. Akaiwa, K. Thornton, and P.W. Voorhees: *J. Comput. Phys.*, 2001, vol. 173, pp. 61–86.
22. R. Duddu, D.L. Chopp, P. Voorhees, and B. Moran: *J. Comput. Phys.*, 2011, vol. 230, pp. 1249–64.
23. X. Zhao, R. Duddu, S.P. Bordas, and J. Qu: *J. Mech. Phys. Solids*, 2013, vol. 61, pp. 1433–45.
24. X. Zhao, S.P. Bordas, and J. Qu: *J. Mech. Phys. Solids*, 2015, vol. 81, pp. 1–21.
25. Y. Wang, L.Q. Chen, and A. Khachaturyan: *Scripta metall. mater.*, 1991, vol. 25, pp. 1387–92.
26. J.W. Cahn and J.E. Hilliard: *J. Chem. Phys.*, 1958, vol. 28, pp. 258–67.
27. P. Leo, J. Lowengrub, and H.J. Jou: *Acta mater.*, 1998, vol. 46, pp. 2113–30.
28. A.M. Jokisaari, S.S. Naghavi, C. Wolverton, P.W. Voorhees, and O.G. Heinonen: *Acta Mater.*, 2017, vol. 141, pp. 273–84.
29. T. Wang, G. Sheng, Z.K. Liu, and L.Q. Chen: *Acta Mater.*, 2008, vol. 56, pp. 5544–51.
30. Y. Tsukada, Y. Murata, T. Koyama, and M. Morinaga: *Mater. Trans.*, 2009, vol. 50, pp. 744–48.
31. J. Kundin, L. Mushongera, T. Goehler, and H. Emmerich: *Acta Mater.*, 2012, vol. 60, pp. 3758–72.
32. L. Mushongera, M. Fleck, J. Kundin, Y. Wang, and H. Emmerich: *Acta Mater.*, 2015, vol. 93, pp. 60–72.
33. J. Zhu, T. Wang, A. Ardell, S. Zhou, Z. Liu, and L. Chen: *Acta mater.*, 2004, vol. 52, pp. 2837–45.
34. M. Cottura, Y. Le Bouar, B. Appolaire, and A. Finel: *Acta Mater.*, 2015, vol. 94, pp. 15–25.
35. Y. Wang and A. Khachaturyan: *Acta metall. mater.*, 1995, vol. 43, pp. 1837–57.
36. M. Gururajan and T. Abinandanan: *Acta Mater.*, 2007, vol. 55, pp. 5015–26.
37. Y. Tsukada, Y. Murata, T. Koyama, and M. Morinaga: *Mater. Trans.*, 2008, vol. 49, pp. 484–88.
38. A. Gaubert, Y. Le Bouar, and A. Finel: *Philos. Mag.*, 2010, vol. 90, pp. 375–404.
39. G. Boussinot, Y. Le Bouar, and A. Finel: *Acta Mater.*, 2010, vol. 58, pp. 4170–81.
40. Y. Tsukada, Y. Murata, T. Koyama, N. Miura, and Y. Kondo: *Acta Mater.*, 2011, vol. 59, pp. 6378–86.
41. N. Zhou, C. Shen, M. Mills, Y. Wang: *Philos. Mag.*, vol. 90, pp. 405–36.
42. P.H. Leo, J.S. Lowengrub, and Q. Nie: *J. Comput. Phys.*, 2000, vol. 157, pp. 44–88.
43. M. Greenwood, J.J. Hoyt, and N. Provatas: *Acta Mater.*, 2009, vol. 57, pp. 2613–23.
44. H. Garcke, B. Nestler, B. Stinner, and F. Wendler: *Math. Models Methods Appl. Sci.*, 2008, vol. 18, pp. 1347–81.
45. A.G. Khachaturyan: *Theory of structural transformations in solids*, 1983.
46. D. Schneider, O. Tschukin, A. Choudhury, M. Selzer, T. Bohlke, and B. Nestler: *Comput. Mech.*, 2015, vol. 55, pp. 887–901.
47. A. Durga, P. Wollants, and N. Moelans: *Model. Simul. Mater. Sci. Eng.*, 2013, vol. 21, p. 055018.
48. M. Silhavy: *The mechanics and thermodynamics of continuous media* (Springer), 2013.
49. A. Karma and W.J. Rappel: *Phys. Rev. E*, 1998, vol. 57, p. 4323.
50. M. Fahrman, P. Fratzl, O. Paris, E. Fahrman, and W.C. Johnson: *Acta Mater.*, 1995, vol. 43, pp. 1007–22.
51. C.A. Bateman and M.R. Notis: *Acta Mater.*, 1992, vol. 40, pp. 2413–31.
52. V. Lanteri, T.E. Mitchell, and A.H. Heuer: *J. Am. Ceram. Soc.*, 1986, vol. 69, pp. 564–69.
53. J. Eshelby: *J. Elast.*, 1975, vol. 5, pp. 321–35.
54. J. Cahn and D. Hoffman: *Acta Metall.*, 1974, vol. 22, pp. 1205–14.
55. Y. Wang, D. Banerjee, C. Su, and A. Khachaturyan: *Acta mater.*, 1998, vol. 46, pp. 2983–3001.
56. J.J. Eggleston, G.B. McFadden, and P.W. Voorhees: *Physica D*, 2001, vol. 150, pp. 91–103.
57. S. Torabi, J. Lowengrub, A. Voigt, and S. Wise: *Proc. R. Soc. A*, 2008, vol. 465, pp. 1337–59.